

Review

Multiscale Modelling Methodologies of Lithium-Ion Battery Aging: A Review of Most Recent Developments

Mir A. Ali ¹, Carlos M. Da Silva ¹ and Cristina H. Amon ^{1,2,*}

¹ Department of Mechanical and Industrial Engineering, University of Toronto, 5 King's College Road, Toronto, ON M5S 3G8, Canada; mirabbas.ali@mail.utoronto.ca (M.A.A.); carlos.dasilva@utoronto.ca (C.M.D.S.)

² Department of Chemical Engineering and Applied Chemistry, University of Toronto, 184 College Street, Toronto, ON M5S 3E4, Canada

* Correspondence: cristina.amon@utoronto.ca

Abstract: Lithium-ion batteries (LIBs) are leading the energy storage market. Significant efforts are being made to widely adopt LIBs due to their inherent performance benefits and reduced environmental impact for transportation electrification. However, achieving this widespread adoption still requires overcoming critical technological constraints impacting battery aging and safety. Battery aging, an inevitable consequence of battery function, might lead to premature performance losses and exacerbated safety concerns if effective thermo-electrical battery management strategies are not implemented. Battery aging effects must be better understood and mitigated, leveraging the predictive power of aging modelling methods. This review paper presents a comprehensive overview of the most recent aging modelling methods. Furthermore, a multiscale approach is adopted, reviewing these methods at the particle, cell, and battery pack scales, along with corresponding opportunities for future research in LIB aging modelling across these scales. Battery testing strategies are also reviewed to illustrate how current numerical aging models are validated, thereby providing a holistic aging modelling strategy. Finally, this paper proposes a combined multiphysics- and data-based modelling framework to achieve accurate and computationally efficient LIB aging simulations.

Keywords: lithium-ion battery aging; battery life; empirical modelling; electrochemical modelling; multiscale modelling



Citation: Ali, M.A.; Da Silva, C.M.; Amon, C.H. Multiscale Modelling Methodologies of Lithium-Ion Battery Aging: A Review of Most Recent Developments. *Batteries* **2023**, *9*, 434. <https://doi.org/10.3390/batteries9090434>

Academic Editors: Pascal Venet, Karim Zaghib and Seung-Wan Song

Received: 23 June 2023

Revised: 12 August 2023

Accepted: 21 August 2023

Published: 24 August 2023



Copyright: © 2023 by the authors. Licensee MDPI, Basel, Switzerland. This article is an open access article distributed under the terms and conditions of the Creative Commons Attribution (CC BY) license (<https://creativecommons.org/licenses/by/4.0/>).

1. Introduction

Nearly 30 years ago, Sony Corporation introduced the rechargeable lithium-ion battery (LIB), which has since gained widespread adoption as a prominent energy storage solution addressing climate change [1]. LIBs are distinguished from competitor battery technologies (e.g., lead acid, nickel metal hydride, alkaline) through key advantages like high working voltages, high specific energy, and long cycle life [2]. These advantages have been recognized by global automakers like Tesla, Volkswagen, Ford, and General Motors (GM), who have been working for several years to optimize battery-powered technology for a new generation of fully electric vehicles (EVs) [3].

The several advantages of LIBs are shadowed by unresolved challenges related to their performance and safety [1]. The persistent degradation over life (i.e., aging) of LIBs is inevitable. In an EV, increased battery aging yields reduced functional life and driving range [4]. Before aging is mitigated, it must be modelled across LIB life. With a pre-existing aging model, battery designers can develop control strategies to minimize battery aging, increase battery life, and optimize driving range.

Aging occurs in two different modes: calendar aging and cycle aging. Calendar aging occurs in the absence of an electric load, whereas cycle aging occurs due to charging/discharging the battery [5]. Despite their differences, cycle aging and calendar aging both irreversibly consume battery capacity through either a loss of lithium inventory (LLI) or a loss of active

material (LAM) [6]. These losses are due to parasitic side reactions driven by LIB operating conditions [2]. In addition to intrinsic aging contributions, extrinsic contributions such as spatio-temporal cell–cell differences in operating parameters (e.g., temperature, current) directly influence individual and neighboring cell aging at the battery pack scale [7]. Thus, to model cell aging, a deep understanding of aging mechanisms involving their contributing physical phenomena is required (e.g., heat generation, stress evolution, electrochemical reaction kinetics).

Aging mechanism effects are delineated through electrochemical-based models employing differential equations that describe governing reactions [8]. Alternatively, LIB aging testing is commonly used to develop empirical models based on aging indicator evolution [8]. The most recent developments in machine learning techniques have also been leveraged to develop adaptive prediction algorithms for LIB aging [8].

Aging reactions occur at the cell scale, but several contributing factors from the battery pack and electrode particle scales directly influence these reactions. Typically, the literature presents aging modelling techniques for cell-scale aging reactions alone. A limited number of reviews discuss aging phenomena modelling strategies considering contributing factors from different hierarchical scales. Herein lies the central motivation of this work.

This paper serves two main purposes. Firstly, it reviews the latest developments in LIB aging mechanisms and modelling techniques, considering factors from multiple hierarchical scales. Secondly, it presents a novel framework for modelling and validating LIB aging. This work aims to contribute to the understanding of aging phenomena and factors at various structural scales, providing valuable insights for hierarchical modelling efforts.

The paper begins by presenting a precursory discussion on heat generation in battery systems as a primary factor governing aging. This is then followed by a multiscale description of battery aging mechanisms, contributing factors, modelling techniques, and testing strategies. It then proceeds to discuss a proposed framework to model and validate multiscale aging effects and is concluded with a discussion on aging research challenges/future perspectives to help advance this field.

2. Heat Generation In Battery Systems

Heat generation and subsequent temperature evolution in LIBs govern aging progression. Parasitic aging reactions proceed due to heat generation from LIB chemical reactions associated with cycling.

There are two types of heat generation within LIBs: reversible heat generation (i.e., entropic) and irreversible heat generation (i.e., joule/ohmic, mixing, active polarization, enthalpy change). Reversible heat generation arises due to cyclic ion diffusion in electrodes, whereas irreversible heat generation is due to permanent physical changes in LIB structure hindering charge transport, diffusion, and ionic concentration distributions [9].

Rising heat generation causes LIB primary reactions to compete with parasitic aging reactions. Moreover, specific temperature ranges can complement both primary and parasitic reactions or favor one over the other, which complicates temperature control [9]. The following subsections detail heat generation sources at different hierarchical scales.

2.1. Electrode Particle Heat Generation Phenomenon

The electrode-particle scale heat generation phenomenon is the foundation for thermal-related aging effects observed at different scales and is directly related to particle morphology. Any feature that hinders diffusion generates heat. Zhang et al. [10] found that heat generation increases with particle radius due to increased resistive or joule heating. This is due to larger particles having increased resistance to lithium-ion diffusion. In contrast, when ellipsoidal particles are used instead of spherical particles, an increase in the aspect ratio decreases particle heat generation. Beyond joule heating, the particle heat generation phenomenon is also influenced by entropic heating, enthalpy change heating, and heat of mixing. Entropic heating is the only form of reversible heat generation caused by the change in the arrangement of lithium ions in the electrode crystal structure during

intercalation/de-intercalation [11]. The enthalpy change heating is due to permanent phase changes in active materials due to lithium-ion diffusion. Finally, the heat of mixing is due to non-homogeneous ion distributions during cycling causing interactions between dissimilar ions [9].

2.2. Battery Cell Heat Generation Phenomenon

Heat generation sources present at the electrode-particle scale have an accumulative effect at the cell scale. For instance, particle-scale overpotentials generate active polarization heating at the electrodes due to lithium ions needing to overcome the charge transfer resistance at the electrode–electrolyte interface. In addition, joule heating through the electrodes and electrolyte causes an overall increase in cell temperature [9].

Heat generation processes presented thus far result from intrinsic LIB phenomena. Extrinsic stress factors also contribute to battery system heat generation and subsequent temperature evolution. However, all heat generation factors are balanced by the battery thermal management system (BTMS), which mitigates extensive temperature fluctuations. BTMS and extrinsic factor impacts on heat generation are discussed in the next section.

2.3. Battery Pack Heat Generation Phenomenon

Scaling up LIBs to the pack scale introduces system variability effects to heat generation [11]. Cell-to-cell variations in temperature arise due to variability in production processes, BTMS effectiveness, and ambient temperature [11,12].

Poor manufacturing tolerance control leads to ineffective homogenization of physical properties [12]. Variations at the electrode production stage lead to reduced porosity of electrode microstructures and subsequent increase in joule heating [11]. Additionally, if the bus bar welding strategy or material composition has large deviations, it leads to increased variable contact resistance with battery cells. This causes uneven current distributions in the battery pack and a subsequent increase in localized joule heating. Moreover, with unequal contact resistances, batteries would show dissimilar state properties, thereby causing increased heat generation [12]. This result is often observed when the state of charge (SOC) is less than 25% and the depth of discharge (DOD) is greater than 75%, where entropic and overpotential heat generation increases, respectively [11].

Beyond manufacturing, BTMS performance and ambient temperature have combined effects on heat generation. Low temperatures coupled with high discharge rates lead to increased heat generation due to higher polarization losses [11]. Conversely, high temperatures accelerate the rate of active material phase changes due to increased ionic diffusion. If the BTMS cannot maintain a 5 °C maximum temperature gradient in the battery pack, localized cell heating effects occur, causing accelerated aging [13].

Localized cell heating is critical because a battery pack's aging is directly proportional to its most aged cell [12]. Failure modes like thermal runaway require only one cell to fail, and through failure propagation, the pack fails as a whole [11].

Heat generation sources at the particle, cell, and pack scales directly influence LIB aging. The particle heat generation sources have accumulative effects at the cell scale. At the pack scale, intrinsic heat generation sources are complemented by extrinsic heat generation factors from manufacturing processes and/or operating environments. Subsequent sections expand on relationships between multiscale temperature evolution and physical aging phenomena.

3. Aging Mechanisms

LIBs have a finite performance life due to several aging mechanisms irreversibly reducing their capacity for an intended application. When battery capacity drops below 80% of the initial value, it is unsuitable for EV applications [14].

To quantify aging, metrics like state of health (SOH—see Equation (1)) and impedance rise are utilized.

$$SOH = \frac{Capacity_{charge/discharge}}{Capacity_{Initial}} \quad (1)$$

Parasitic aging reactions causing irreversible capacity losses exist only at the cell scale. However, there are several contributing factors from the electrode particle and battery pack scales that promote these reactions. Figure 1 shows a schema relating contributing factors to cell aging phenomena at the battery pack and electrode particle scales.

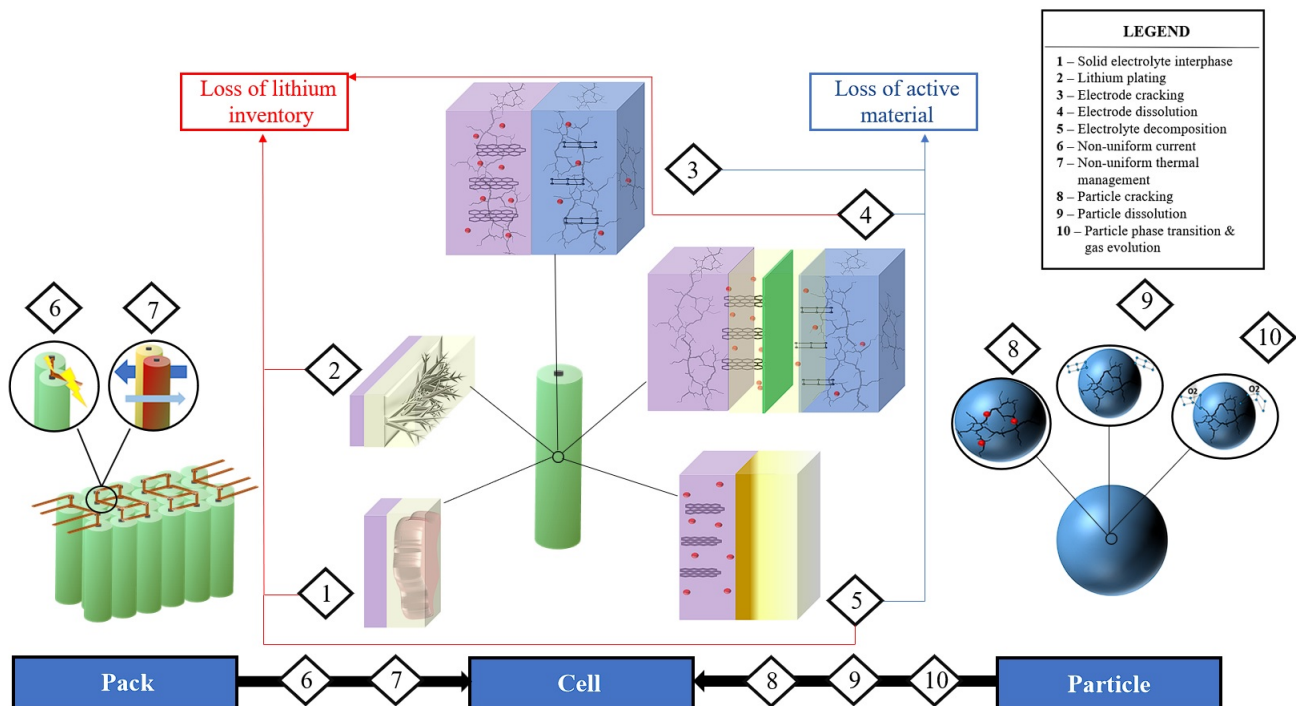


Figure 1. Lithium-ion battery aging schema relating contributing factors at the pack and particle scales to aging mechanisms at the cell scale.

Cell aging mechanisms along with contributing factors at different hierarchical scales are discussed in the subsequent sections.

3.1. Electrode Particle Aging Contributing Factors

Many aging mechanisms arise from the electrode particle scale and are primarily due to the intercalation and de-intercalation of lithium ions. Intercalation-induced stress is positively correlated with lithium-ion concentration due to an increase in electrode elastic modulus [10,15]. As particles stiffen, their porosity decreases, causing increased resistance to lithium diffusion and subsequent reductions in power output [15]. Electrode particles also become more prone to cracks and subsequent LAM during high-voltage cycling or high cycling rates. During high-voltage cycling, inhomogeneities form in the electrode particle lattices as evidenced by inactive domains, which then cause cracks to form. Increased cycling rates (i.e., >1C) generate increased inactive regions, and subsequently cause more cracks [16]. As more cracks form over time, electrode materials lose their mechanical strength, fracture, and cause battery failure [17]. Although cracks propagate and cause LAM, minor cracks can have beneficial effects on battery operation. Trevisanello et al. [18] described how polycrystalline cathode materials form minor cracks within secondary particles, thereby enabling electrolyte infiltration. This decreases the charge transfer resistance and increases the diffusion coefficient by one order of magnitude. Single

crystalline cathode materials, however, do not crack, and although they have a longer cycle life, they show kinetic rate limitations at low potentials and capacities.

Beyond particle cracking, particle dissolution also causes adverse aging effects. Dissolved electrode particles attach to the non-dissolved electrode surface and generate overpotentials due to the hindrance of lithium-ion diffusion. In addition, they also consume lithium ions, leading to capacity fade through LLI. To quantify the capacity loss, Lee et al. [19] showed that 200 ppm of manganese from a lithium manganese oxide (LMO) cathode present in the electrolyte reduces the cathode capacity by nearly 15%.

Electrode material decay and ultimate dissolution at the particle scale begins with material phase transition. For instance, at low levels of lithiation, nickel-rich cathodes (e.g., NMC811) undergo phase transitions from layered structures to disordered spinel and finally, to rock salt structures. These structures lack the ability to reversibly intercalate lithium and thus irreversibly decrease battery capacity [20].

Electrode material phase transitions are accompanied by oxygen gas evolution. The presence of oxygen (O_2) causes side reactions with the electrolyte to form additional gases such as carbon monoxide (CO) and carbon dioxide (CO_2) [20]. Beyond electrolyte decomposition, if gas evolution is not mitigated, it increases the risk of a battery explosion and subsequent thermal runaway [21].

Aging factors observed at microscopic scales have macroscopic effects at higher hierarchical scales. The translation of these observations at the cell and pack scale are presented in subsequent sections.

3.2. Battery Cell Aging Mechanisms

Aging mechanisms occur during the entire life cycle of the battery, from production to cycling and storage stages. This section covers the aging mechanisms in each of these stages.

3.2.1. Production-Related Aging Mechanisms

LIB production has several steps that introduce aging when the cell is first cycled. Each step introduces different aging mechanisms that have a range of effects on cell performance over life.

The first step in cell production is forming active materials through mixing. The mixing and formation of the electrode slurry have implications on particle size and solid phase conductivity. With improper mixing, the final product will have scarce electrode materials, leading to increased charge transfer resistance and subsequent joule heating. Strict control protocols on mixing speeds, durations, and impeller tip sizes are enforced to ensure an optimal quantity and size distribution of electrode particles [5].

The electrode materials are then coated onto current collectors and calendared. This process has implications for electrode porosity, thickness, and density. Insufficient calendaring results in non-uniform active material thickness, pockets of lithium deposition in the anode, and subsequent dendrite formation. Furthermore, if particle porosity is suboptimal, there would be added resistance to lithium-ion diffusion and a subsequent increase in joule heating [5].

The last step before the electrolyte is filled involves cutting, winding/stacking, and welding active material layers to form a jelly roll for cylindrical cells and a stack for pouch cells. If performed ineffectively, material fragments contact the oppositely charged electrode during cycling and cause internal short circuits [5].

In addition to short circuit risks, Bank et al. [22] revealed how the practice of oversizing the anode material leads to a passive electrode effect. Concentration and voltage gradients are formed, causing the lithium ions to transition between the anode passive and active regions. This leads to sporadic trends of increased/decreased capacity that hinder battery performance consistency.

The last step in the production process is forming, where the finished cell is cycled several times at reduced C-rates to form a stable solid-electrolyte interphase (SEI) layer.

This step is intended to insulate the electrolyte from electrons; however, it consumes lithium ions in the process and leads to LLI [5].

To minimize production-related aging mechanisms, cell-scale battery manufacturing processes must have strict control measures. For instance, the air dew point is kept at $-50\text{ }^{\circ}\text{C}$ to prevent water in the production environment from mixing with the electrolyte [5]. If water mixes with the electrolyte, hydrofluoric acid (HF) forms and subsequently dissolves cathode transition metals [23].

Without strict control measures, increased battery aging begins at the onset of production. These symptoms are precursors to the calendar and cycle aging mechanisms discussed in the following sections.

3.2.2. Calendar Aging Mechanisms

Calendar aging is most relevant in applications where idle duration exceeds operational duration. It is influenced by three primary factors: time, SOC, and temperature [24,25]. However, the influence of temperature on calendar aging is more pronounced than SOC. Werner et al. [24] demonstrated that cells stored at $60\text{ }^{\circ}\text{C}$ reached the same level of capacity fade in 3 weeks as cells stored at $50\text{ }^{\circ}\text{C}$ reached in 8 weeks despite having a 45% difference in SOC.

Keil et al. [6] performed a calendar aging study showing that capacity fade and resistance generally increase with temperature. Regarding SOC, capacity fade has a plateau region of 20–30% followed by a sharp rise at approximately 60–70%. These results are due to the low potential of the graphite anode in a highly lithiated state, causing electrolyte reduction and subsequent SEI formation. This effect is aggravated by temperature since increased temperatures ($>40\text{ }^{\circ}\text{C}$) accelerate electrolyte reduction reaction kinetics. Additionally, as the electrolyte is reduced, it reduces the potential for fast charging due to increased resistance to lithium-ion transport in both the electrolyte and electrodes [26].

When considering internal resistance, ohmic and polarization resistances predominantly cause a rise in cell impedance during calendar aging [25]. This aligns with expectations, since a physical barrier hinders lithium-ion transport across the cell along with subsequent charge transfer reactions. This internal resistance rise, however, plateaus at approximately 130 days of storage regardless of temperature or storage SOC [27].

Beyond the SEI layer, Chabaz et al. [28] found that at high SOC, cathode material degrades substantially due to the thermal instability of certain cathodic compositions (e.g., lithium cobalt oxide, or LCO) in low-lithiated states.

To minimize calendar aging effects, storing LIBs at lower temperatures ($<40\text{ }^{\circ}\text{C}$) and reduced SOC ($<50\%$) is recommended. Under these conditions, capacity gains of up to 2.42% over life for lithium titanate oxide (LTO) chemistries are demonstrated [28].

3.2.3. Cycle Aging Mechanisms

LIB cycling involves transporting lithium ions and corresponding electrons to both sides of the cell. The compounding effects of intercalation/de-intercalation at the particle scale cause local deformation, phase change, and volume change of active materials at the cell scale. For instance, graphite exhibits a 10% volumetric change with intercalation, whereas silicon exhibits a 310% volumetric change. Volumetric changes cause active material fatigue. In the short term, this leads to sporadic power/conductivity losses due to reduced contact with current collectors [29]. In the long term, the electrode material fails, leading to LAM and eventual cell failure [29].

Mechanical stress within a LIB is not constrained to intercalation/de-intercalation processes alone. SEI layer formation introduced in Section 3.2.1 produces several gases that further compound cell mechanical stresses. Moreover, mechanically induced cracks on the surface of active materials and/or the SEI layer itself give rise to new sites for SEI-forming reactions and subsequent capacity fade [29].

Apart from the SEI layer, hindrances to lithium-ion diffusion are also caused by lithium dendrite formation/lithium plating. Dendrites are formed on the anode surface when

lithium-ion concentration in the liquid phase exceeds that in the solid phase. Dendrite growth leads to irreversible capacity fade through LLI and poses safety risks if contact is made with opposing electrodes [2]. Furthermore, dendrite formation has been shown to cause non-linear capacity fade due to decreased porosity at the anode/separator interphase followed by a sharp impedance rise [30]. Conditions inducing dendrite formation include battery overcharging, fast charging, and cold temperature (<0 °C) charging. During overcharging or fast charging, the electrode reaches a fully lithiated state faster, causing the remaining ions to form dendrites [2,31]. Under cold temperatures, dendrite growth occurs due to reduced kinetics of lithium-ion diffusion [32,33].

Beyond capacity fade and safety concerns, lithium plating and SEI formation also have deteriorating effects on the battery electrolyte. Due to the electrolyte species being consumed in the formation of these products, its ionic conductivity decreases, resulting in increased polarization within the LIB [11]. This is a consequence of the reduced electrolyte salt stability at low/high temperatures and high potentials causing the electrolyte to degrade and subsequently be consumed [11,34,35].

Most aging mechanisms observed at the anode are also observed at the cathode [2]. Active material phase transition, dissolution, fatigue, and cathodic electrolyte interphase (CEI) formation all occur with similar mechanisms observed at the anode. Cathode dissolution is most detrimental to cycle performance since it increases internal resistance along with LAM. Additionally, high mechanical stress is observed at the cathode with increased DOD, where DOD width is more significant than the upper and lower limits [2]. Zhu et al. and Leonardi et al. [36,37] found that besides LLI, cathode degradation is the most dominant LIB aging mechanism during cycling due to repeated lithium-ion diffusion causing high anisotropic strain and subsequent fracture of metal oxide particle structures. Ryu et al. [38] further identify cathodic chemistry as the main cause of this behavior. When the nickel stoichiometric fraction exceeds 0.8, there is an abrupt anisotropic shrinkage/expansion that de-stabilizes internal microcracks, causes propagation to the surface, and creates channels for electrolyte penetration and subsequent LAM.

LIB aging is commonly defined as a function of cathodic chemistry. Preger et al. [39] performed a cycle aging study where lithium nickel cobalt aluminum oxide (NCA), lithium nickel manganese cobalt oxide (NMC), and lithium iron phosphate (LFP) batteries were compared based on DOD, discharge rate, and temperature. LFP cells had the longest cycle life compared to the other chemistries across all conditions. However, the performance gap is significantly reduced when considering the lower discharge energy, capacity, and voltage of the LFP chemistries as compared to NMC or NCA. Consequently, stronger dependency exists on DOD and SOC for NMC and NCA chemistries vs. LFP. Additionally, LFP exhibits an increasing rate of capacity fade in the temperature range of 15–35 °C, whereas NMC exhibits a decreasing rate, demonstrating the effect of different dominating aging mechanisms at this temperature range.

All aging mechanisms discussed thus far occur in the first life of an EV. After a SOH of 80%, the second life of an EV battery begins. Martinez-Laserna et al. [40] studied the viability of batteries that were retired from primary application and used for a grid-scale PV plant in two application programs: residential demand and power smoothing. They concluded that regardless of the reduced demand in the second life, if the point of non-linear aging (i.e., a “knee point”) is reached in the first life, then the batteries will not be viable in the second life. To evaluate the occurrence of this knee point, Braco et al. [41] conducted accelerated second life cycle testing on a Nissan Leaf module and concluded that if the estimated error between the experimentally determined and predicted battery internal resistance exceeds 3%, the knee point has been reached. These findings yield a large window for the viability of LIB second life. Casals et al. [42] estimated that the second life of the battery ranges from 8 to 20 years, independent of chemistry.

Figure 2 provides a graphical summary of a LIB lifetime trajectory for aging events.

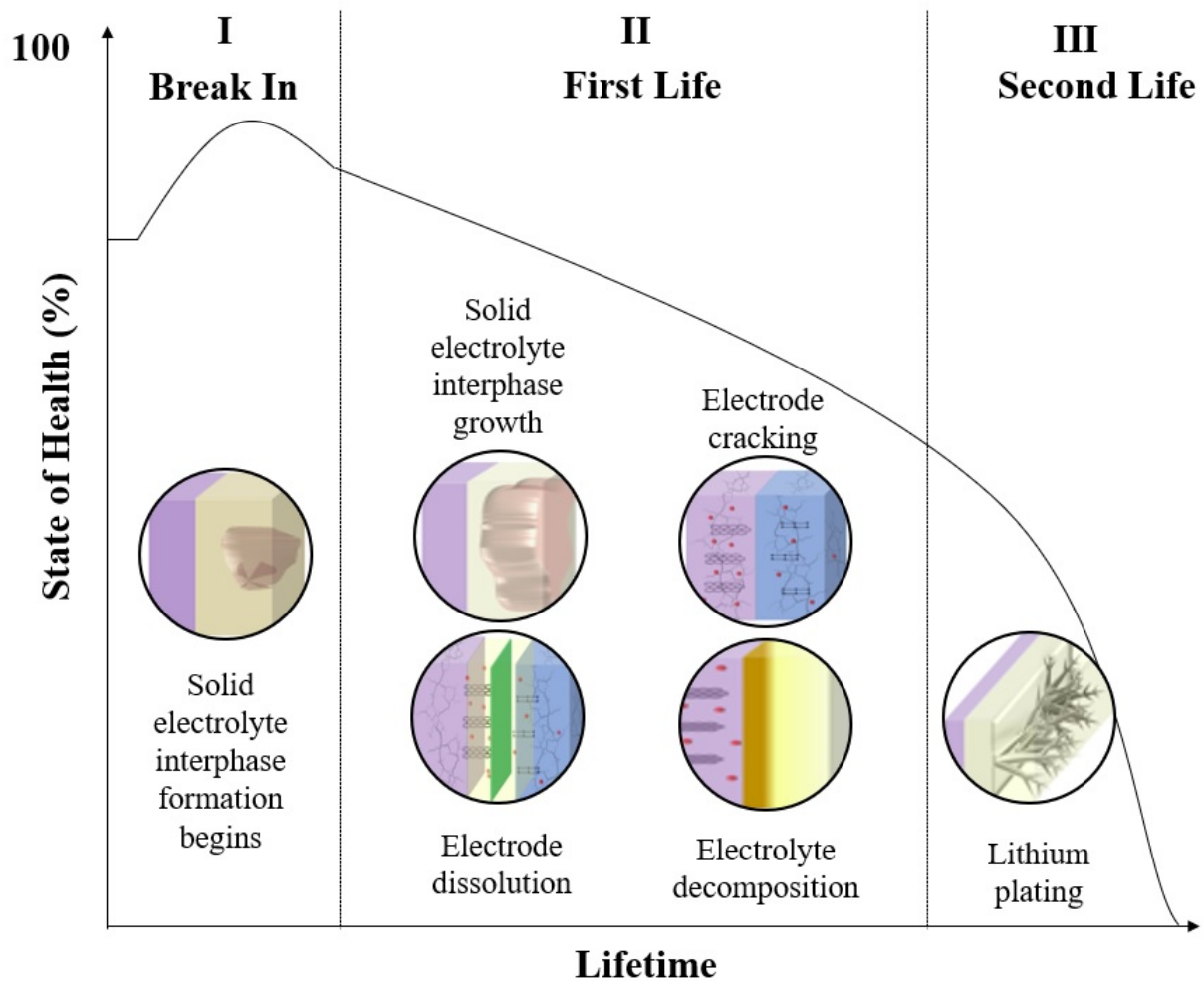


Figure 2. Typical evolution of state of health and aging mechanisms during battery lifetime.

Stage I depends on manufacturing conditions. Cells experience an increase in capacity in the initial cycles if manufactured with variable lithium quantities. However, capacity does begin to decrease during the formation phase of manufacturing due to SEI formation. In stage II, aging mechanisms like SEI growth, electrode cracking, electrode dissolution, and electrolyte decomposition ensue at a quasi-linear rate. In stage III, SOH diminishes non-linearly due to the increased rate of lithium plating [5,11]. It should be noted that the distinction between different aging stages has been defined in this paper by the evolution of different aging mechanisms. In reality, a battery's first life and second life are defined by application requirements, which have variable regions along the curve.

3.3. Battery Pack Aging Contributing Factors

At the pack scale, LIB aging contributions are due to the intrinsic variability of the cell composition, extrinsic stress factors, and usage patterns.

3.3.1. Cell Spreading

Intrinsic cell-to-cell variation in the battery pack is defined as "spreading" [11], causing variable aging paths of cells. Zheng et al. [43] found that variable LLI in the cell composition causes accelerated system performance aging. As mentioned in Section 2.3, a battery pack is only as effective as its most aged cell since the failure of one cell can "spread" to others. Hence, intrinsic variation in aging rates causes the largest influence on pack utilization [44]. The effect of intrinsic variations in aging rates is a drift in cell voltage and current as a conse-

quence of varying cell resistance. Potential consequences of these variations include the overcharging/discharging of cells during cycling conditions, as outlined in Section 3.2.3 [43–45].

The cause of the internal resistance variation is attributed to variations in LIB composition due to poor manufacturing tolerances (as described in Section 3.2.1) or extrinsic stress factors causing variations in cell properties. In the following sections, a discussion on extrinsic factors along with usage pattern impacts is presented.

3.3.2. External Stress Factors

When batteries are integrated into application architectures, their performance is impacted by their surroundings and operating modes. The most influential external factor to battery utilization is the application BTMS. Yuksel et al. [46] conducted a plug-in hybrid electric vehicle (PHEV) simulation study to relate LIB aging in different climates with the impact of BTMS operating on forced convection air cooling. Without cooling, aggressive driving (e.g., high accelerations) in hot regions (e.g., Phoenix, USA) cut battery life by 2/3. Furthermore, battery life was found to be 73–94% longer in mild-temperature regions (e.g., San Francisco, USA) due to reduced demand on the battery pack for cabin conditioning. When air cooling is used, battery life increases by a factor of 1.5–6 depending on the driving regimen employed. Thus, the addition of a BTMS is critical in keeping batteries at stable operating temperatures (i.e., between 25 and 50 °C) [11]. Although air cooling substantially improved battery life in this application, it may not be the most optimal option for a BTMS. Liquids have higher heat transfer coefficients than air, which heightens their effectiveness at removing residual battery heat [9].

Apart from the BTMS, application operating conditions also have an impact on aging. Regenerative braking causes short recharge periods of high current rates, which are hypothesized to degrade the battery system. However, Keil et al. [47] conducted a 5-month cycle study which revealed that increased regenerative braking reduced battery aging by decreasing lithium plating, as the DOD reduced with increased recovered charge.

3.3.3. User Patterns Impact

In an EV application, user patterns are defined by factors such as driving speed, acceleration, driving range, highway vs. city driving times, and auxiliary usage [48]. Mueller et al. [48] conducted a user simulation study showing that at the maximum normal distribution of these values, capacity fade rapidly approaches the 80% remaining capacity target in under 4 years. Liu et al. [49] experimentally validated that going from a maximum speed of approximately 82 km/h to 120 km/h diminishes vehicle mileage over life by nearly 19%. Jafari et al. [50] found that with aggressive driving habits (i.e., higher accelerations), battery packs expend up to 45% more energy than non-aggressive driving habits. It is apparent that adopting aggressive driving patterns causes accelerated rates of the aforementioned aging mechanisms. Approaching the end of life in an accelerated time frame diminishes EV reliability compared to competing technologies. Thus, considering user patterns is essential when modelling LIB aging.

The aging mechanisms and multiscale contributing factors discussed in this section are shown to have compounding effects on the life and performance of a LIB. These mechanisms and factors must be modelled and subsequently mitigated in advance of their occurrence to optimize LIB performance and extend life. A variety of different multiscale modelling techniques are discussed in the following section.

4. Aging Modelling Strategies

An effective LIB aging model should satisfy the following requirements:

1. Model the cycle and calendar aging phenomena together;
2. Reference electro-chemo-mechanical-related aging phenomena;
3. Be scalable to multiple hierarchical scales;
4. Validated experimentally under realistic operating conditions;
5. Implementable online in a battery management system (BMS).

Two main types of models aim to achieve these objectives: empirical data-based models and mechanistic multiphysics-based models. The data-based models rely on pre-existing data to develop correlations, whereas the multiphysics-based models rely on solving a set of electrochemical governing equations to gauge battery performance. This section will discuss both model functions and most recent developments.

4.1. Data-Based Models

Data-based modelling develops correlations within an existing dataset. Examples of this type of model include empirical models, equivalent circuit models, machine learning models, deep learning models, and statistical models.

4.1.1. Empirical Models

Empirical models create correlations based on experimental trends. These correlations either model key battery aging metrics or sub-parameters that directly affect aging (e.g., temperature).

Xia et al. [51] presented a stochastic capacity degradation model coupled with Arrhenius temperature dependency and a dynamic response impedance model to represent cycle aging from data obtained experimentally. The following equations define this stochastic capacity degradation model [51]:

$$\zeta(T, Ah) = \sum_i^E \zeta \delta(T) Ah = \sum_i^E \left(\delta \zeta_{ref} e^{\left(\frac{-E_a}{R} \left(\frac{1}{T} - \frac{1}{T_{ref}} \right) \right)} \right) Ah \tag{2}$$

$$\delta \zeta_{ref}(SOC_{avg}, SOC_{dev}) = k_{s1} SOC_{dev,i} e^{k_{s2} SOC_{avg,i}} + k_{s3} e^{k_{s4} SOC_{dev,i}} \tag{3}$$

$$SOC_{avg} = \frac{1}{\Delta Ah_m} \int_{Ah_{m-1}}^{Ah} SOC(Ah) dAh \tag{4}$$

$$SOC_{dev} = \sqrt{\frac{3}{\Delta Ah_m} \int_{Ah_{m-1}}^{Ah} (SOC(Ah) - SOC_{avg})^2 dAh} \tag{5}$$

where

- ζ : capacity degradation at non-ambient conditions;
- $\zeta \delta(T)$: capacity degradation at ambient temperature T ;
- SOC_{avg}, SOC_{dev} : average SOC, deviation from average SOC;
- Ah : charge;
- $k_{s1}, k_{s2}, k_{s3}, k_{s4}$: empirically derived coefficients.

To model impedance rise, it was observed that capacity and impedance are linearly correlated up until 80% residual capacity. Therefore, the two parameters (a and b) could be defined using the following Equation (6):

$$R_{ref} = a \zeta(T, Ah) + b \tag{6}$$

where the slope and intercept ((a, b) , respectively) are determined from experimental data. However, impedance is not contingent solely on capacity fade. Factors such as temperature also have implications for cell impedance. Thus, Equation (6) is modified to add an Arrhenius temperature dependency, as shown in Equation (7) [51].

$$\frac{1}{R(\zeta, T)} = \frac{1}{a \zeta + b} e^{-\frac{E'_a}{R} \left(\frac{1}{T} - \frac{1}{T_{ref}} \right)} \tag{7}$$

where E'_a describes the experimentally determined impedance.

In an alternative method, Maheshwari et al. [52] modelled cycle aging by creating separate empirical models based on stress factors like C-rate and SOC and then summed the

total aging contributions. Suri et al. [53] used their cumulative cycle aging models to create severity maps for different combinations of operating conditions while Werner et al. [24] conducted similar analyses using the Arrhenius temperature dependency for modelling calendar aging. It is noted, however, that adding aging mechanism contributions could yield errors since each mechanism does not have an equivalent contribution to aging.

When combining aging models, cycle and calendar aging are typically modelled separately and then added. DeGennaro et al. [54] superimposed several calendar and cycle aging models together and subtracted a residual capacity loss value assuming 15% capacity loss from first life. They scaled this model to the pack scale by assuming homogeneous cell aging and fit it according to the data in the TEMA EU database. Assuming homogeneous cell aging, however, is not representative of the cell-spreading effects seen in battery packs. Xu et al. [55] created individual empirical models for battery aging and added up their respective effects in a dynamic test cycle. Although the superposition of aging models has been practiced extensively in the literature, subsequent sections will show that it inaccurately gauges aging effects by not considering aging path dependency.

Beyond the Arrhenius equation, other methodologies such as the Eyring law are used to define temperature-related effects. Redondo-Iglesias et al. [56] expand the Arrhenius equation to other stress factors using the Eyring law defined by Equation (8).

$$C_a(T, SOC) = AT^n e^{-\frac{E_a}{kT} + B_1 S_1 + \frac{C_1 S_1}{kT}} \quad (8)$$

where C_a is the capacity fade rate, n is the temperature exponent, k is the Boltzmann constant, B_1 is the direct influence factor of S_1 , and C_1 is the interaction factor between S_1 and temperature. This expression expands to multiple different stress factors to capture all factors that influence aging as opposed to solely looking at temperature with Arrhenius relationships [56].

Building on the ability to simultaneously capture multiple aging factors, Galatro et al. [57] summarized Mathieu et al.'s findings, where capacity fade was first fit to a kinetic constant, k_c , and time factor, α , followed by fitting the kinetic constant to a quadratic equation defining the dependency on different stress factors. The capacity fade model is presented in Equation (9) and the kinetic constant correlation is presented in (10) [57].

$$\ln \left[-\ln \left(\frac{C(t)}{C_0} \right) \right] = \ln(k_C) + \alpha \ln(t) \quad (9)$$

$$\ln(k_C) = \beta_0 + \beta_T \frac{1}{T} + \beta_S SOC + \beta_C I_C + \beta_D I_D + \beta_{TC} \frac{I_C}{T} + \beta_{TD} \frac{I_D}{T} + \beta_{TT} \frac{1}{T^2} + \beta_{SS} SOC^2 \quad (10)$$

where the subindices of the β coefficients are named after the corresponding stress factors: temperature (T), SOC (S), charge (C), and discharge (D). Galatro et al. [57] fit these models and coefficients to four different combined calendar and cycle aging tests and found that the k_C and α values vary drastically with cell chemistry. This study highlighted the importance of correlating models based on chemistry dependency as opposed to generalizing the fitting parameters of one chemistry.

When considering empirical models in the presence of BTMS, optimization strategies such as Pontryagin's principle must be used in conjunction with the aging model to balance energy management/performance with battery aging [58,59].

Although empirical models are developed with experimental studies, they do not capture the internal LIB aging phenomena. Equivalent circuit models (ECMs) address this requirement and are discussed in the next section.

4.1.2. Equivalent Circuit Models

The ECM describes LIB internal operation by quantifying the electrochemical phenomena occurring in the cell. ECMs relate cell performance data to representative electrical

circuit elements that act as analogs for battery internals. Nikolian et al. [60] applied this principle by developing and validating a cell-scale second-order Thevenin ECM.

The ECM can also model battery pack dynamics. If the ECM is presented at the cell scale, multiple circuits can be connected in series and/or in parallel to assess the aging of different battery pack configurations. Using this strategy, Su et al. [61] developed a splice ECM for a vehicle battery pack, while Ding et al. [62] scaled up and improved the Thevenin model.

To accurately represent battery pack architectures, battery parameters are varied either manually or through statistical techniques to capture cell-to-cell differences. Hosseinzadeh et al. [63] combined multiple first-order ECMs in a modular configuration and manually introduced variations to gauge performance. Results revealed that interconnection resistance variation has the most significant impact on cell-to-cell differences, where a 25% resistance variation leads to 22% current dispersion. Escobar et al. [64] also combined several first-order ECMs in conjunction with an Arrhenius-based model to gauge long-term performance of battery packs and BTMSs to joule heating. To account for cell–cell variation, they performed a series of Monte Carlo simulations to simulate variations in beginning of life (BOL) cell capacity and impedance for all pack cells. This work was unique since it combined aging effects with a BTMS controller and was able to establish operating conditions that reduced mean maximum pack temperature by 7% and mean lifetime BTMS energy consumption by 10%. Zilberman et al. [44] used a Monte Carlo simulation to simulate distributions in capacity, impedance, and reversible self-discharge to generate three different battery packs where each cell in the packs was represented by a first-order ECM. They concluded that variation in intrinsic aging rates has the greatest impact on pack utilization and voltage imbalances.

Despite the insight into internal battery dynamics, the ECM fails to make predictions on conditions lacking experimental data. Learning a current dataset to make predictions on conditions that have not been tested requires machine learning strategies, which are discussed in the following section.

4.1.3. Machine Learning Models

Machine learning strategies model the dynamic LIB system by allowing computers to learn data and improve their model performance without the need for additional programming. These strategies, coupled with aging mechanism knowledge, create a LIB “digital twin”. In the cyber-physical system where the twin exists, machine learning modelling techniques enable closer interaction between the physical and digital embodiment of the battery along with smarter aging control strategies and subsequently longer lifetimes [8].

To perform machine learning modelling, a pipeline approach is employed (see Figure 3).

Machine learning techniques have been used extensively in the literature for intelligent state estimation, SOH prediction, gauging remaining useful life trajectory, and aging mechanism identification from characteristic test profiles. These techniques are ideal for handling large datasets typical of aging tests and harnessing digital twin innovations to intelligently control batteries in EVs.

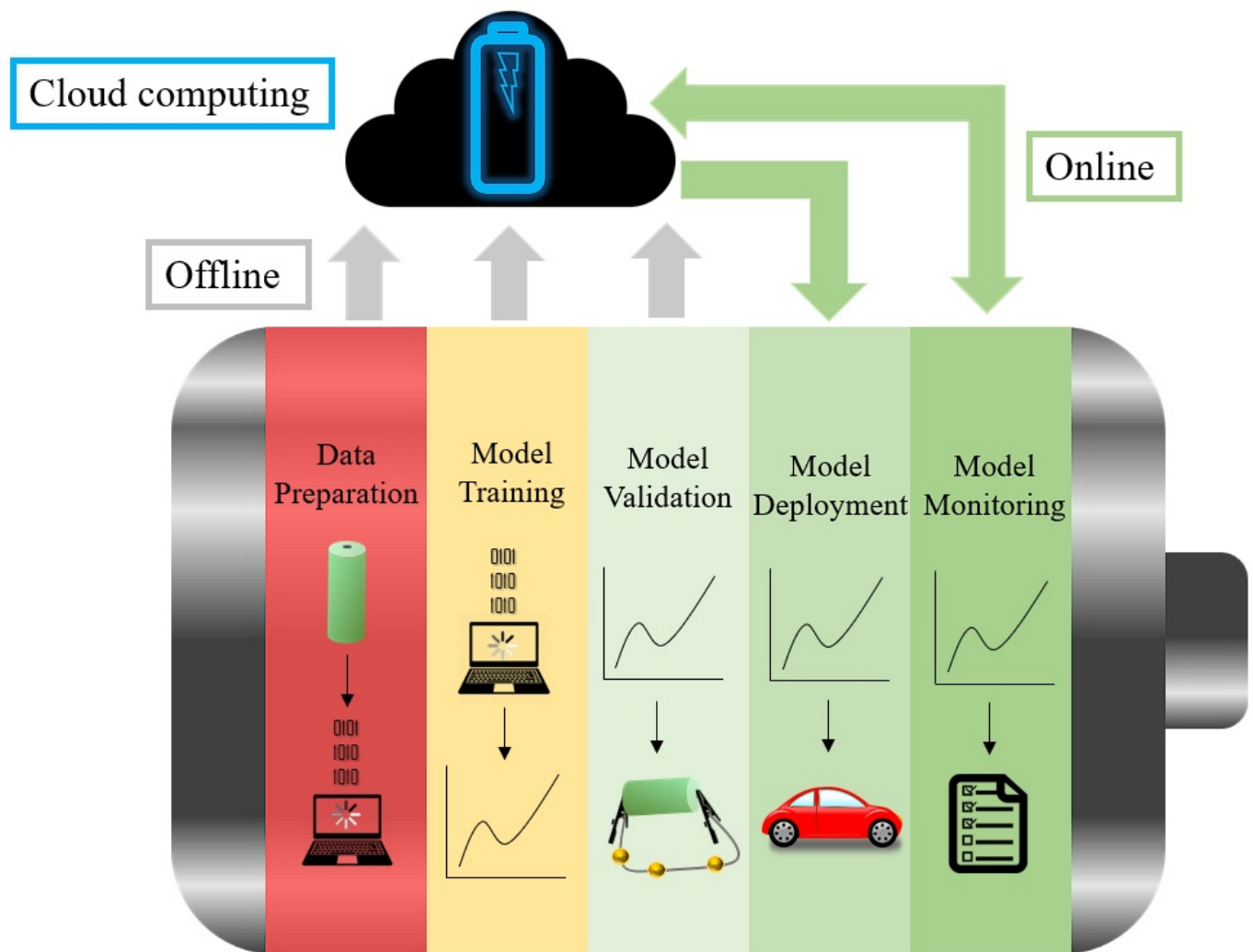


Figure 3. Machine learning model development stages, where offline stages are stored in the cloud and online stages are deployed in the electric vehicle.

At the electrode particle scale, machine learning strategies assess the heterogeneity of electrode lattices that cause crack formation or assess the thermodynamic stability of particle morphology. Mao et al. [65] used K-means clustering and Euclidean symmetry to assess the oxidation gradient across a nickel-rich cathode material for isolating higher-oxidation zones in the bulk of the particle (i.e., inactive domains). To examine the thermodynamic stability of dopant materials in tackling dendrite formation, Liu et al. [66] employed a support vector machine (SVM) algorithm to classify thermodynamically stable configurations coupled with kernel ridge regression (KRR) to estimate reaction energy at the dopant–electrode particle interface.

At the cell scale, machine learning modelling techniques are applied to measured SOH data to make predictions on the remaining battery life. Roman et al. [67] employed a pipeline approach to estimate the SOH of various LIB formats during cycling using four different models including random forest, deep neural network ensemble, Bayesian ridge regression, and Gaussian process regression. Li et al. [68] used random forest regression to extract parameters from constant current–constant voltage (CC–CV)-tested cells characterized by incremental capacity (IC) analysis. As an alternative to IC analysis, Zhang et al. [69] collected 20,000 electrochemical impedance spectroscopy (EIS) spectra at different SOHs for input to a Gaussian regression model to predict the LIB remaining useful life. Son et al. [70] presented an integrated framework for SOH estimation through multiphysics feature extraction during CC–CV testing. The evolution of mechanical and

electrical parameters was used to extract features and develop a Gaussian process regression model with a non-linear quadratic kernel. Li et al. [71] used a linear regression analysis based on measurements from microscopic images of lithium deposition to generate a safety boundary index map that envelops all safe battery design conditions.

Apart from evaluating cell aging, machine learning is also used to detect the presence of specific aging mechanisms. Chen et al. [72] implemented a decision tree algorithm to detect the presence of lithium plating by training their model on multiple electrochemical signatures and detecting the presence of the non-linearity in signature evolution.

In contrast to the common offline model training strategy, Liu et al. [73] developed a relevant vector machine model to predict the remaining useful life of the battery while being trained online. This was accomplished by discarding non-support vectors before retraining the model to reduce model memory and subsequently, computational requirements.

Machine learning techniques can also be applied to cells that have been retired from their primary application to assess effectiveness in secondary applications. Ni et al. [74] used the Levenberg–Marquardt method to extract parameters from a prognostic mechanistic model and fed them into a support vector regression model that was improved by moth flame optimization. This model was then trained on residual capacity tests of 1000 retired cells from bus applications and achieved a root mean square error (RMSE) of 2.18% by using just 10% of the test data. In another method, Johnen et al. [75] applied a sigmoidal regression technique to model cycle aging in first life and beyond.

At the pack scale, machine learning models introduce LIB variability and associated aging effects. Weng et al. [76] scaled up a first-order ECM model for a cell to a module consisting of three parallel cells and a pack consisting of thirty cells, with each cell having manually manipulated capacity and resistance values to account for cell spreading and extrinsic variations. Using partial charging data and support vector regression-generated IC peaks, the model demonstrated capacity fade and resistance rise along with SOH evolution. Zhou et al. [77] applied a k-nearest neighbors regression technique by incorporating data from all cells in the battery pack and determining the remaining useful life of a cell from a weighted average of several surrounding cells with similar aging trajectory. To evaluate pack SOC, Deng et al. [78] employed Gaussian process regression by taking data from all cells in the pack and providing a probability distribution.

A key disadvantage of machine learning modelling is the large volume of data required to build a coherent model. Accelerated aging testing is a method to achieve required aging states in a shorter period of time while accumulating fewer data points [57]. In the absence of this regimen, aging must be detected in early test cycles. Severson et al. [79] trained a regularized linear elastic net on 100 cycles of the discharge voltage curve, which generated a 9.1% error on capacity fade later in life. This is attributed to detecting a shift in voltage at constant capacity, which indicates LAM. Fei et al. [80] used a machine learning pipeline strategy with a wrapper method feature selection technique to extract features from raw charge and discharge data and subsequently fed them into six different models. Furthermore, RMSE of the lifetime prediction estimation from the first 100 cycles was reduced from 173 to 115 cycles when compared to existing work. Kong et al. [81] used partial charge–discharge curves and the difference method to extract voltage-dependent health features along with measuring battery surface temperature. These features were fed into a Gaussian process regression model yielding an RMSE of 1% in all capacity estimations and 5% in all remaining useful life estimations. Diao et al. [82] employed ensemble learning to model the early detection of anomalous aging behavior in production lots of cells with the aim of qualifying them based on pre-existing, qualified lots.

Machine learning modelling techniques provide several different methods to evaluate LIB aging and its contributing factors at different hierarchical scales. Despite their demonstrable success, they struggle with more complex and dynamic tasks (e.g., identifying aging mechanisms with microscopic images). For these tasks, deep learning methods are employed.

4.1.4. Deep Learning Models

Deep learning involves the use of algorithms such as neural networks where each node represents a neuron, and the arrows represent connections from the output of one neuron to the input of the other [83]. Figure 4 presents how a network is constructed in the context of battery aging.

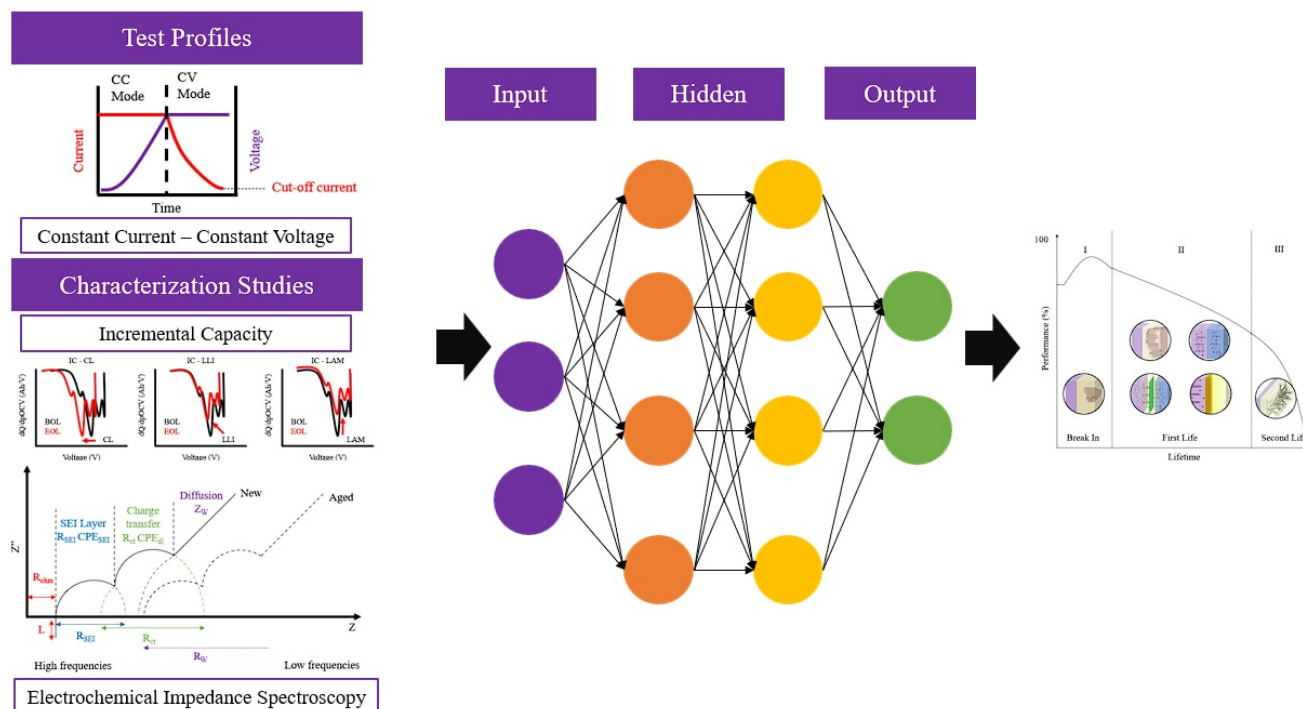


Figure 4. Battery aging neural network workflow: input typical test profile/characterization studies and output an aging trajectory model.

Neural networks offer higher layers of complexity and abstraction as compared to other machine learning techniques, thus handling more complex and dynamic tasks.

At the electrode particle scale, neural networks analyze microscopy images and gauge cell heterogeneity, which leads to electrode fracture. Qian et al. [84] used convolutional neural networks (CNNs) to identify mismatched regions of valence and strain in nickel-rich cathode materials. High-valence, low-strain regions were associated with inactive domains caused by microcracks, whereas low-valence, high-strain regions were associated with surface cathode degradation. Jiang et al. [85] applied a CNN to nano-tomographic slices of composite electrodes and positively correlated detachment of electrode particles from the carbon binder with an increase in charging rate. Bhowmik et al. [86] applied a recurrent neural network (RNN) to an extensive data cohort to generate an SEI rendering along with its interactions with battery active particles.

At the cell scale, deep learning methods are employed to diagnose aging mechanisms by extracting electrochemical features or to predict remaining useful life. Lee et al. [83] used an artificial neural network (ANN) to identify the % of LAM for each electrode and LLI. Electrochemical features were extracted from incremental capacity/differential voltage (IC/DV) curves to train the network, with a resulting RMSE less than 0.1. They also conducted a similar study by mapping partial charge and discharge curves into likelihood vectors to simulate various aging conditions. These likelihood vectors were then fed into an ANN to produce a failure index that classified failure likelihood. Using this model, thermal runaway was predicted in advance of its occurrence [87]. Ruan et al. [88] created a generalized CNN that could rapidly diagnose aging mechanisms through feature extraction from synthetically created half-cell data. The model was able to predict and quantify aging mechanisms in 0.012 s without the need to run long-term aging experiments for a training

dataset. In an alternative approach, Chun et al. [89] use a deep reinforcement learning strategy to accurately predict the stoichiometric range of a LIB. This strategy gauges aging by looking at the diminishing stoichiometry over the life of a LIB as opposed to using classic indicators like SOH.

To predict LIB remaining useful life and long-term capacity fade dependencies, Zhang et al. [90] employed a long short-term memory (LSTM) RNN trained on CC-CV data of LIB cells used independently of offline data. Assefi et al. [91] were able to combine calendar and cycle aging using an LSTM RNN by separately extracting calendar and cycle aging features. Liu et al. [92] used the same network combined with Gaussian process regression to estimate the remaining useful life. The LSTM fits the residuals, whereas the Gaussian process regression fits the intrinsic mode function while providing uncertainty measurements.

Due to the complexity of neural networks, they can be difficult to develop without any prior knowledge of the system's behavior. Transfer learning offers a solution to this problem by leveraging the use of existing architectures for performing similar predictions [93]. Azuke et al. [93] used a transfer learning technique to leverage NMC calendar aging testing data and network architecture to predict the capacity fade of LFP cells with a 1.01% error. Tang et al. [94] proposed an alternative strategy where a base model describing capacity decay over time with existing data is established and then transformed by input–output slope bias correction to capture target cell aging. The capacity fade of four different types of cells was modelled using this method, with RMSE being less than 2.5%. Takyi-Aninakwa et al. [95] used a transfer learning technique to develop an LSTM to accurately predict the SOC of a LIB.

Deep learning methods have also been applied at the battery pack scale to predict the SOH or gauge cell-to-cell differences. Song et al. [96] predicted the SOH of a battery pack using a feed-forward network trained and validated on a repository of one-year operating data for electric vehicles in Shanghai, China. Che et al. [97] generated universal health indicators from CC-CV pack testing to train an ensemble of neural networks in predicting SOH. Shu et al. [98] presented a different approach in gauging cell spreading by presenting a two-stage model that employs an LSTM to find the mean SOH of the pack and then determines the differences between cell SOH and mean SOH.

There have also been examples of online implementations of deep learning methods. Shen et al. [99] proposed a CNN for online cell-scale capacity estimation using voltage, current, and charge capacity measurements during a partial charge cycle. Khalegi et al. [100] implemented a nonlinear autoregressive exogenous neural network model that was trained offline using a ten-year cycle dataset of 21 LIB cells. This predicted the SOH on untrained data acquired online with an RMSE of 0.46.

Deep learning modelling methods are shown to model aging by using several layers of abstraction on complex datasets. However, there are instances when parameters of interest (e.g., SOC, SOH) cannot be directly measured, and thus, a neural network cannot be applied. For these conditions, statistical models are applied to evaluate LIB aging.

4.1.5. Statistical Models

Statistical models are employed when parameters of interest cannot be measured directly. Alternative parameters along with noise are introduced into these models to obtain a probability distribution of the desired parameters. One example of this technique is the Kalman filter, which recursively predicts the value of a state variable using measurable variables. Smiley et al. [101] presented a multiple-model Kalman filter which generated a probability mass function. This specified the probability that each of the models considered best represents the cell under observation. Xu et al. [102] also explored the characterization of aged LIBs by using a sigma point Kalman filter alongside an LSTM network to predict the SOC of an aged battery pack. Yang et al. [103] presented a multi-time scale extended Kalman filter model scaled up from a second-order ECM that predicts the SOC and capacity of pack cells.

An alternative method to the Kalman filter is the particle filter. Both methods are similar in operation; however, the latter is applicable to nonlinear and non-Gaussian processes. Tang et al. [104] proposed the use of a gradient correction particle filter to predict LIB cell capacity fade under CC-CV operation with gradient correction regulated by a base model. Meng et al. [105] used a particle filter alongside empirical mode decomposition (EMD) to predict LIB end of life (EOL) and its associated uncertainty. Their work proved to be significant since it forecasts LIB EOL in advance of its occurrence while preventing overfitting in their extrapolations.

As a consequence of LIB random behavior, stochastic processes are also used to model their aging. The Monte Carlo method, for example, is used as a stochastic approach to capture the random yet probabilistic variations of battery parameters. Kannan et al. [106] conducted Monte Carlo simulations followed by sensitivity analyses to correlate the variability of 18650 LIBs and phase change material (PCM) operating parameters (i.e., melting temperatures) with safety considerations at stressed conditions (i.e., unsafe event probability). Rogers et al. [107] modelled capacity evolution by simulating a random population of cells. Lin et al. [108] presented a compositional prognostic-based model using the Monte Carlo simulation and a gamma process to observe the likelihood of test batteries failing, based on defined failure thresholds.

Apart from the Monte Carlo method, Wang et al. [109] use the Wiener stochastic process coupled with the Copula function to analyze the reliability of a LIB pack and the dependency between its cells. Galatro et al. [7] implemented a three-parameter non-homogenous gamma process to model LIB aging while accounting for cell spreading. Lai et al. [110] predicted the LIB remaining discharge energy (RDE) by employing a hidden Markov model to predict the future load, along with experimental testing to evaluate SOC at different temperatures, and a forgetting factor recursive least square algorithm (FFRLS) to update parameters.

Information entropy is an alternative method to quantify information distribution and discrete characteristics to evaluate information randomness and chaos. The more information there is, the larger the degree of uncertainty and/or randomness a system will have. An ideal application of this is the assessment of battery inconsistency within pack formats. Duan et al. [111] applied information entropy in this context by analyzing parameters such as capacity, internal resistance, and CC-CV charge capacity ratio to assess the inconsistency of a twelve-cell battery pack.

Empirical data-based models are shown to predict aging with pre-existing data. However, they do not present many details regarding the aging phenomena governing LIB aging. To capture these phenomena, multiphysics-based models are used.

4.2. Multiphysics-Based Modelling

To model aging phenomena, mechanistic, multiphysics models must be employed. These models are represented by a series of differential equations to represent constituent or energy balances that describe the cell's physical and chemical processes. The differential equations are approximated to give system properties, followed by experimental validation. Multiphysics models are of different degrees of granularity and can directly model processes acting at the particle and electrode scales [29]. There are three common model types: pseudo-two-dimensional models (P2D), single-particle models (SPM), and thermal models. This section discusses the details and provides the most recent developments for each model.

4.2.1. Pseudo-Two-Dimensional Model

The P2D model was developed in 1993 by Doyle et al. [112] using a combination of porous electrode theory and concentrated solution theory. This model serves as the reference for all internal LIB processes, and thus, all other proposed models are simplifications [113]. Although it is the most comprehensive electrochemical model, it is also the most computationally expensive. There are more than sixty physical parameters in the

P2D model [114]. Furthermore, to solve its partial differential equations, mesh generation and numerical iterative calculation on two spatial dimensions of polar plate thickness and particle radius are required [115].

Electrodes in the P2D model are a porous matrix composed of spherical particles surrounded by the electrolyte solution. Intercalation/de-intercalation of lithium ions occurs through the surface area of these particles with uni-directional transfer processes [116]. Figure 5 presents a graphic describing the P2D model configuration.

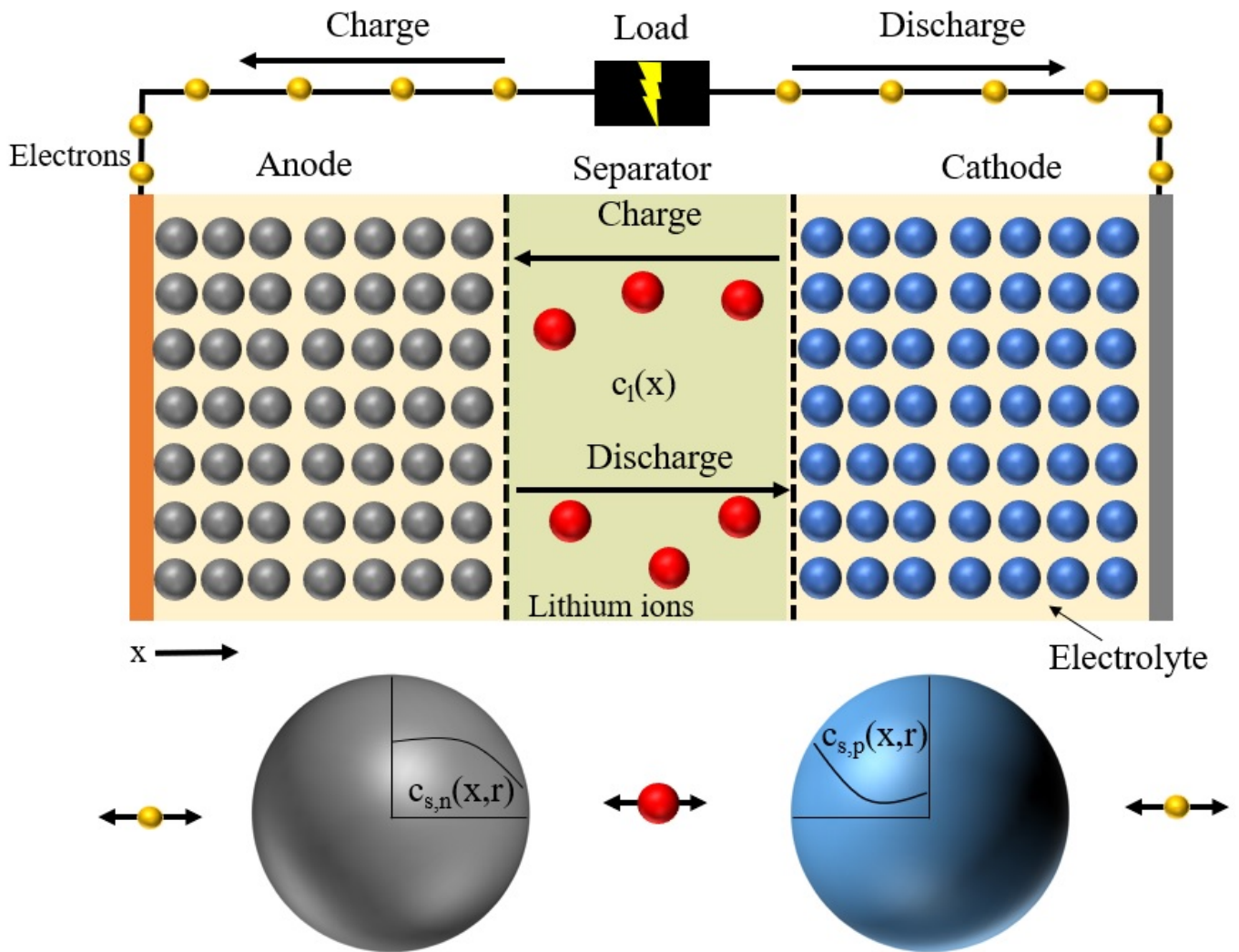


Figure 5. Pseudo-two-dimensional model graphical summary showing ion transport in cell and particle domains.

The governing equations for the P2D model are as follows [112,116,117]:

Electrodes:

$$\frac{\partial c_{s,k}(x, r, t)}{\partial t} = \frac{D_{s,k}}{r^2} \frac{\partial}{\partial r} \left(r^2 \frac{\partial c_{s,k}(x, r, t)}{\partial r} \right) \tag{11}$$

$$\epsilon_k \frac{\partial c_{e,k}(x, t)}{\partial t} = \frac{\partial}{\partial x} \left(D_{eff,k} \frac{\partial c_{e,k}(x, t)}{\partial x} \right) + a_k(1 - t_+) J_k(x, t) \tag{12}$$

$$\sigma_{eff,k} \frac{\partial^2 \phi_{s,k}(x, t)}{\partial x^2} = a_k F J_k(x, t) \tag{13}$$

$$-\sigma_{eff,k} \frac{\partial \phi_{s,k}(x,t)}{\partial x} - \kappa_{eff,k} \frac{\partial \phi_{e,k}(x,t)}{\partial x} + \frac{2\kappa_{eff,k}RT}{F}(1-t_+) \frac{\partial \ln c_{e,k}}{\partial x} = I \quad (14)$$

$$J_k(x,t) = K_k (c_{s,k}^{max} - c_{s,k}^{surf})^{0.5} (c_{s,k}^{surf})^{0.5} c_{e,k}^{0.5} \left[\exp\left(\frac{0.5F\mu_{s,k}(x,t)}{RT}\right) - \exp\left(-\frac{0.5F\mu_{s,k}(x,t)}{RT}\right) \right] \quad (15)$$

$$\mu_{s,k}(x,t) = \phi_{s,k}(x,t) - \phi_{e,k}(x,t) - U_k; V_{cell}(t) = \phi_{s,k}(0,t) - \phi_{s,k}(L,t) \quad (16)$$

Separator:

$$\epsilon_k \frac{\partial c_{e,k}(x,t)}{\partial t} = \frac{\partial}{\partial x} \left(D_{eff,k} \frac{\partial c_{e,k}(x,t)}{\partial x} \right) \quad (17)$$

$$-\kappa_{eff,k} \frac{\partial \phi_{e,k}(x,t)}{\partial x} + \frac{2\kappa_{eff,k}RT}{F}(1-t_+) \frac{\partial \ln c_{e,k}}{\partial x} = I \quad (18)$$

The key features of these equations are solid-state lithium-ion concentration (c_s), derived from Fick's law of diffusion for spherical particles; liquid-state lithium-ion concentration in the electrolyte and separator (c_e), given by lithium-ion conservation; solid-state potential (ϕ_s), from Ohm's law; liquid state potential (ϕ_e), determined from Kirchoff's and Ohm's laws; and lithium-ion pore wall flux (J), determined by the Butler–Volmer kinetics equation [116].

The P2D model uses particle-scale processes to model aging observed at the cell scale. Smiley et al. [118] presented a multiple reduced-order P2D model framework at different aging states to simulate an interacting multiple-model environment, coupled with a Kalman filter, to select which model best matches the current battery dynamics. Lv et al. [119] used the P2D model to simulate the aging trajectory of a LIB and separate the data based on linear and non-linear regions. This modelling technique is effective as it captures the non-linearity of aging separately as opposed to struggling to capture both regions with a single correlation. Chen et al. [120] applied a P2D model to study LIB aging in pristine and partially aged states due to SEI formation and LAM. Carelli et al. [121] scaled up a P2D model to a P3D model to study the coupling of SEI layer formation and lithium plating. Through their analysis, they were able to develop aging maps that indicated the most critical degradation conditions based on C-rate and temperature—the worst of which being $>3C$ and $<-5^\circ C$. O'Kane et al. [122] used the P2D model to analyze the interdependency of lithium plating, particle cracking, and SEI layer formation in graphite electrode particles. This work is one of few that relates aging mechanisms together as opposed to modelling them separately.

The P2D model is also used to model battery pack property variations. Ashwin et al. [123] extended this model to a battery pack of four cells to predict the effects of differential cell aging during constant voltage cycling, while capturing the effect of current imbalance. Xia et al. [124] scaled up a P2D model at the cell scale and combined it with thermal, series/circuit, SEI formation, and fluid dynamics models to gauge EV battery pack life. Rumpf et al. [125] assessed the influence of cell–cell variation by combining a P2D cell model with several other physical models. They found that an asymmetric orientation of cells in a battery pack significantly impacts current variance due to connector resistances. Yang et al. [126] modeled the unbalanced discharging and aging due to temperature differences in a parallel configuration by combining a scaled-up P2D model at the cell scale with a 2D thermal model.

Couplings of the P2D or similar multi-dimensional models better capture aging phenomena. Mendoza et al. [127] performed an electrochemical–mechanical simulation of the LIB cathode material in response to cathodic intercalation/de-intercalation reactions. The electrochemical model consisted of volumetric equations solved in the particle and electrolyte domain, whereas the mechanical model relied on the quasi-static conservation of linear momentum. At the particle scale, Lee et al. [128] used the P2D model and an

electrochemical side reactions model to determine the effect of dissolved cathode ions on the graphite anode. Similar sandwiched 2D electrode models were also used to gauge the intercalation-related mechanical stress on electrode particles by analyzing inhomogeneous current distributions [129]. Despite its inherent advantages, the P2D model fails to capture the heterogeneity in an electrode, which causes localized failures [130]. To capture these phenomena, higher-fidelity models are required (e.g., 3D finite-element models).

4.2.2. Single-Particle Model and Other Simplified Electrochemical Models

The increased number of variables and partial differential equations (PDEs) required to be solved in the P2D model adds significant computational complexity and hinders its online implementation. To remedy this, mathematical manipulations, along with a series of assumptions, are applied to reduce the model order. Rodriguez et al. [131] proposed the following four different methods to develop high-fidelity discrete-time state space reduced-order models (ROMs) to subsequently provide the electrochemical variables of interest when studying aging:

1. Discrete-time realization algorithm (DRA) that converts functions to discrete-time unit pulse responses, and then uses either the Ho–Kalman or the eigensystem realization algorithm to generate an ROM;
2. Continuous time realization algorithm (CRA) that converts the function to a continuous time state space model and then to a discrete-time state space model;
3. Hybrid realization algorithm (HRA) that converts functions to discrete-time frequency response and then reduces the model order;
4. Lagrange interpolation realization algorithm (LRA) that converts functions to a continuous state space model which approximates function values followed by a reduction in order and conversion to a discrete state space model.

Each method yields similar results. Thus, particular strategies are selected depending on computing memory and execution time requirements [131].

Another way to simplify the P2D model is to omit a set of its variables. The single-particle model (SPM) only uses Equations (11)–(15) of the P2D model as its governing equations, and has two primary assumptions: electrodes are modelled as two spherical particles, and variations in electrolyte concentration, along with subsequent potential differences, are ignored. The SPM is applicable to all systems that do not have thick electrodes and/or fast charge/discharge ($>1C$) rates [116]. Modifications to the SPM model to accommodate these drawbacks have been made, such as the SPM+ model and improved SPM+ model (ISPM+). The ISPM+ model approximates the value of physical parameters through correlations and assumes the degree of electrode polarization and solid-state diffusion is the same for both electrodes. It also neglects the effects of temperature on parameter evaluation at room temperature. These simplified models are then used to assess LIB aging modes through their parameter determination [115].

Lyu et al. [132] presented an in situ aging modelling technique for LIB cells using an SPM with parameter identification occurring through activation and response analyses. Wang et al. [133] proposed a simplified electrochemical model based on the SPM to model the electrochemical behavior of large format LIB cells for a wide range of temperatures ($-10\text{ }^{\circ}\text{C}$ to $45\text{ }^{\circ}\text{C}$) by using excitation group analysis and multi-group particle swarm optimization to evaluate model parameters. Li et al. [134] used an extended SPM model (similar to ISPM+) coupled with an adaptive cubature Kalman filter to predict the SOC of aged LIBs. Ouyang et al. [135] developed a mechanistic prognostic model defined by Equations (19)–(21) to model the dynamic capacity degradation of a large format LIB.

$$V_{simu} = V_{cathode}(y) - V_{anode}(x) - IR \quad (19)$$

$$x = x_0 + \int_0^t \frac{I}{Q_{an}} d\tau \quad (20)$$

$$y = y_0 + \int_0^t \frac{I}{Q_{ca}} d\tau \quad (21)$$

where anode and cathode voltages are measured by assembling half cells with x and y as anode and cathode SOC, respectively, and Q as half-cell capacity. Coupled with an IC analysis, the ability to define SOC in terms of capacity dynamically updates the simulated voltage with every capacity change, thereby tracking aging. In an alternative approach, Smith et al. [136] presented a reduced-order model framework composed of a series of sub-models for each aging mechanism that can model capacity fade in calendar, cycle, and mixed aging regimes.

Simplified electrochemical models are typically combined with thermal and/or mechanical frameworks to provide a more comprehensive representation of aging [137]. Qi et al. [138] studied the overcharging of a LIB pack by combining a thermal abuse model along with a 1D electrochemical model. The electrochemical model receives average temperatures from thermal abuse models and provides the heat generation rate. Chen et al. [139] combined a 1D electrochemical model with a 2D thermal model to study the effects of active air and PCM cooling on pack cycle life. Yamanaka et al. [140] linked an SPM and thermal model through thermal resistance, heat generation, and heat capacity parameters to study the aging phenomena in a LIB pack. Tran et al. [141] combined a reduced-order P2D model using the Pade approximation with a 1D thermal model to study aging in large format cylindrical cells. Song et al. [142] coupled an electro-thermal model to study non-uniform aging due to a temperature distribution in a pouch cell.

Simplified electrochemical models have also been applied at the pack and module scales to study cell–cell variation. Liu et al. [143] used an SPM to study cell–cell variations in a LIB pack and found that if the cells with the largest impedance are placed closest to the load point, cell–cell current distribution is homogenized. Tian et al. [144] studied the inconsistency of parallel connected battery modules using an extended SPM. The extended SPM was generated using the Pade approximation along with the first-order Taylor series expansion.

4.2.3. Thermal Modelling

Thermal and electrochemical model coupling was alluded to in Section 4.2.2, where the latter model uses the temperature data from the former to evaluate heat generation rate from battery operation. This is then fed to the thermal model, which evaluates the temperature, and the cycle repeats, as summarized in Figure 6.

To predict temperature, thermal models use a series of energy balance equations which are discretized to provide parameters of interest, such as average temperature or temperature distributions. Mesh generation discretizes more complex 2D and 3D systems to solve equations over smaller, computationally efficient domains. The coupling of these models presents a more reliable dataset on battery safety and performance [116].

Zhao et al. [4] developed a 2D electro-thermal model to study the thermal gradients induced by tab and surface cooling of a LIB. They found that surface cooling reduces the LIB average temperature, but leads to large thermal gradients at high C-rates. Conversely, tab cooling leads to lower thermal gradients, but a higher average temperature due to reduced heat removal. Jia et al. [145] developed a 0D thermal model in conjunction with modified Arrhenius equations to study the propagation of thermal runaway in LIBs. Mevawalla et al. [146] used a modified 1D coupling of an electrochemical and thermal model to study temperature variations as a function of SOC and C-rate in a prismatic cell. Abada et al. [147] developed a 3D electro-thermal model that also included a 0D calendar aging model to study the critical temperatures for thermal runaway in fresh and aged cells. Reaching the onset temperature for calendar-aged cells is slower than fresh cells due to a larger presence of an SEI layer hindering diffusion of lithium ions.

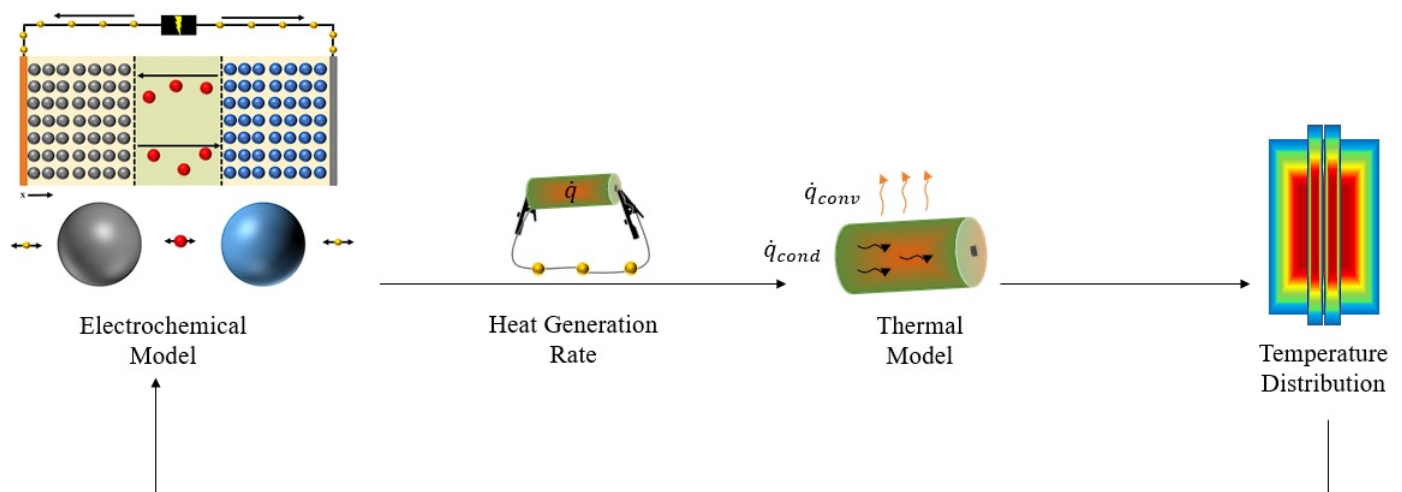


Figure 6. Electrochemical and thermal model coupling methodology to gauge thermal performance by linking heat generation rate and temperature distribution between models.

Thermal modelling at the pack and module scales is also presented in the literature. Jia et al. [148] used the representative volume element (RVE) strategy to develop a thermo-mechanical model which predicts internal short circuits. Hosseinzadeh et al. [149] presented a 1D electrochemical–thermal model for a large format pouch cell and combined it with an electrical circuit model to study the cell–cell variations in parallel configurations. Through this study, variations were found at higher load currents and interconnection resistances. Kang et al. [13] used a thermal model to analyze the temperature distribution of the surroundings in a square- and rectangular-shaped battery pack with cylindrical cells. Chalise et al. [150] presented solutions for thermal conduction and convection that are coupled to study the conjugate heat transfer of a coolant-based LIB pack. Lamrani et al. [151] presented a simplified thermal model to study the effects of a PCM in a battery pack.

Multiphysics models reveal battery aging phenomena with the highest level of detail. However, their increased computational complexity hinders the opportunity for online implementation. It is clear then that an ideal modelling solution should consist of a combined framework of both data- and multiphysics-based modelling techniques.

4.3. Combined Modelling Techniques

Both data- and multiphysics-based models provide means to predict battery aging. On their own, each model carries drawbacks and advantages. An optimal solution for an aging model combines the best features of each model into one coupled framework. Typically, this coupling entails the use of data-based models to predict electrochemical model parameters and use electrochemical results to make predictions.

Kim et al. [152] used a deep Bayesian neural network to estimate the optimized parameter set for the P2D model and used those parameters to solve the set of PDEs. The network alleviates the difficulty in solving the P2D equations, while developing a model that captures all the battery aging phenomena. Li et al. [153] noted advantages when using an ECM in conjunction with a 3D thermal model. The ECM evaluates heat generated from the various internal resistance sources, and feeds it to the thermal model to evaluate temperature distributions at both cell and pack scales. Gottapu et al. [154] presented a thermal model for temperature distribution using an ECM at the pack scale for ohmic heat calculations and natural convection. Zheng et al. [155] coupled a process control technique in the PI observer to a 1D electrochemical model for co-estimation of SOC, capacity, and resistance for a LIB cell. Xia et al. [156] combined a 3D electric–thermal flow model, a stochastic capacity fade model, and a Markovian reliability model to assess the reliability of a battery pack design. Li et al. [157] used the decision tree, support vector machine,

and ANN to model the safety envelope of pouch-cell batteries with data from an FEM. Zhang et al. [158] combined a 1D electrochemical model with a 3D thermal model to study the temperature distribution in a cylindrical cell. Through their study, they found that cylindrical cells have large temperature gradients in the radial direction. In an alternative approach, Tu et al. [159] developed a framework where an SPM model fed battery state information to a neural network to predict cell voltage. This strategy yielded significantly more accurate results than using either model individually. Appiah et al. [160] took a different approach to combining different models by performing a sensitivity analysis on the P2D model parameters. Their analysis identified a number of parameter pairs that had the most pronounced effects on cell degradation.

5. Battery Testing Strategies

Experimental/real-world datasets are required to either train or validate a model. This section presents different types of experimental strategies to obtain such data, the parameters of interest, and the techniques to uncover aging phenomena occurring within a battery system.

5.1. Test Types

Dubarry et al. [161] demonstrated that the best practice for LIB testing involves performing a series of different tests in the following order:

1. Formation or characterization tests to diagnose cell initial prognostics and variations;
2. Duty cycle test to test the battery under the desired condition;
3. Reference performance test (RPT) to characterize parameter evolution for the battery.

This section will discuss these test types in further detail.

5.1.1. Characterization Tests

Characterization tests are performed at the beginning of any testing regimen to establish cell functionality, as well as periodically throughout testing to evaluate the evolution of battery performance (i.e., analogous to RPT) [161]. These tests involve charging and discharging the battery at an established condition and comparing performance parameters to manufacturer values [161]. A common test method used for this type of characterization is CC-CV charge followed by a CC discharge. Figure 7 demonstrates the CC-CV charging process.

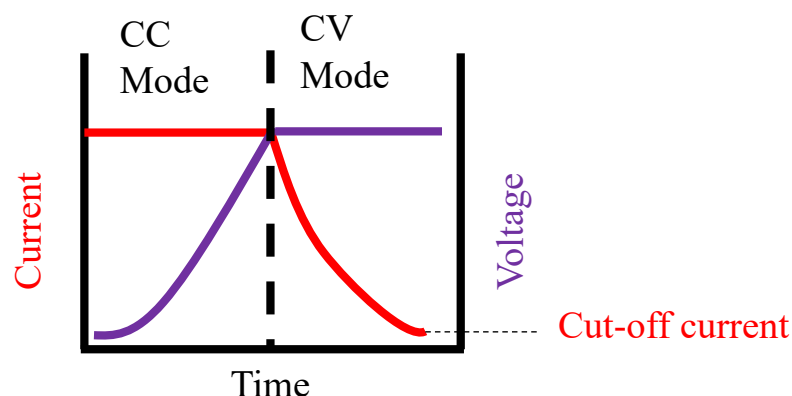


Figure 7. Constant current-constant voltage (CC-CV) battery current and voltage profiles.

To illustrate how this protocol is typically performed, Braco et al. [41] used a CC current of $C/3$ and a cut-off current of $C/33$ for their characterization tests. Before switching over to discharge mode, there is a rest period of approximately one hour to allow the cell to reach equilibrium. The capacity and internal resistance are then measured with cycling hardware.

Beyond capacity and internal resistance evaluation, this testing regimen also yields the open circuit voltage (OCV) vs. SOC curve. Dubarry et al. [161] showcased that if the current during charge and discharge is low enough (i.e., C/25), the voltage can be averaged and taken as a pseudo-OCV (pOCV). Figure 8 demonstrates this process.

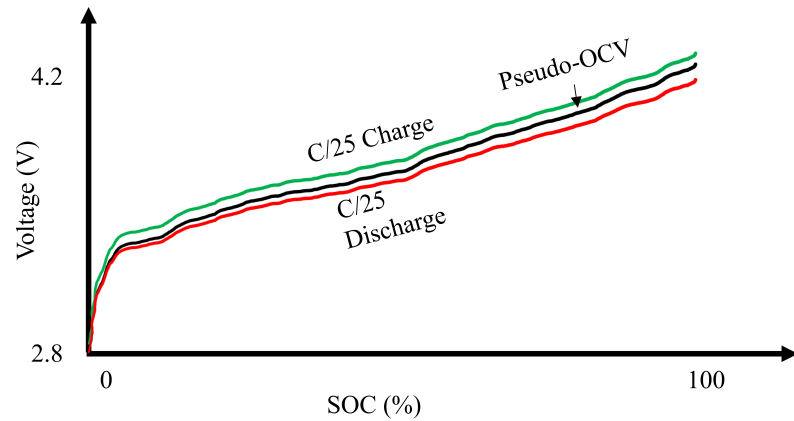


Figure 8. Generation of pseudo-open circuit voltage curve by averaging low C-rate charge and discharge curves (adapted from [161]).

The charge/discharge rate is kept low since the OCV is meant to be a voltage measurement without a load. Furthermore, when plotted against SOC, this curve assesses thermal equilibrium properties. This procedure is repeated for multiple temperatures [44].

To evaluate dynamic properties such as power capability at different SOCs, strategies such as hybrid pulse power characterization tests (HPPC) are employed [40]. Figure 9 presents this test.

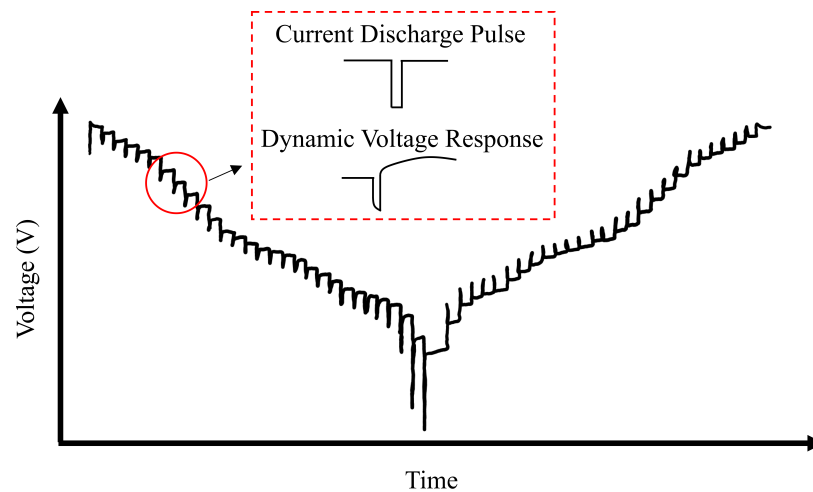


Figure 9. Hybrid pulse power characterization test voltage profile.

This section summarized the testing strategies to evaluate battery prognostics throughout life. The next section will discuss tests that emulate battery operation.

5.1.2. Aging Emulation Testing

To emulate aging, LIB aging mechanisms need to be replicated in experimental environments. For EVs, testing protocols must reflect application usage, and thus, duty cycle style testing is employed. There are two primary types of duty cycles: real and synthetic.

Real duty cycles are based on real-world collected data capturing information reflecting the performance of battery systems and extrinsic factors. Despite representing real-world performance, real driving data age batteries slowly due to lower-than-average values of operating parameters (e.g., discharge current). Baure et al. [162] found that the

average discharge current can be up to 25% lower for real driving data as compared to synthetic data, leading to approximately 86% longer cycling lifetime. This hinders LIB development, as longer lifetimes generate longer test times to capture aging. Pfriem et al. [163] showed that nearly 3 years were required to collect sufficient real data to capture aging.

Synthetic drive cycles take components of real driving data and artificially create a representative test cycle to mimic vehicle performance. Common synthetic cycles include dynamic stress tests (DSTs), federal urban driving schedules (FUDSs), new European driving cycles (NEDCs), and the world harmonized light duty vehicles test procedures (WLTPs). Baure et al. [162] compared the capacity loss caused by cycling testing using DST, FUDS, and NEDC vs. real-life data. None of the synthetic profiles were able to reproduce the long lifetimes of the real driving cycles due to the higher average discharge current. Beyond discharge current, Pfriem et al. [163] found that real drive cycles also exhibit shorter distances, durations, maximum speeds, and average speeds compared to synthetic cycles. Furthermore, EVs are found to adhere to more urban dynamic driving conditions with multiple accelerations. This behavior is not observed in synthetic cycles and can cause discrepancies in aging emulation. There also exist applications where EVs supplement grid distribution of electricity (V2G). Wang et al. [164] demonstrated that the aging from V2G operation is inconsequential compared to realistic driving combined with calendar aging.

The long lifetime challenge from real-world data is overcome through testing acceleration strategies. This preserves driving profile integrity while achieving experimental results in a timely manner. Lee et al. [87] experimented with mechanical bending, dent, and swelling tests to simulate LIB mechanical failure modes. This method, however, does not consider path dependency and aging evolution. Conversely, Diao et al. [165] performed a factorial design of experiment intended to identify optimal accelerated cycle testing conditions for cells considering three stress factors: ambient temperature, discharge current rate, and charge cut-off C-rate. Findings revealed that only the ambient temperature can be used to accelerate battery aging. A test condition at 60 °C, 1C discharge rate, and C/40 cut-off current accelerated aging by a factor of 6, which, in this study, translated to saving a month of testing. With the combination of the test acceleration strategy coupled with real-world driving data, a realistic and optimized emulation of LIB aging can be achieved.

5.2. Aging Phenomena Diagnosis Techniques

LIB characterization testing gauges battery parameter evolution over life. However, to connect these parameters to internal battery aging phenomena, additional diagnostic strategies are required. The most common strategies are EIS and IC/DV analysis.

5.2.1. Electrochemical Impedance Spectroscopy

In EIS, a small current or voltage sinusoidal signal is applied to a battery at different frequencies, after which the response is measured. The results are converted to the frequency domain and then plotted on a Nyquist plot. To specifically model battery kinetic processes, the Nyquist plot is fitted to an ECM. Figures 10 and 11 present the relationship between the Nyquist plot and an ECM [166].

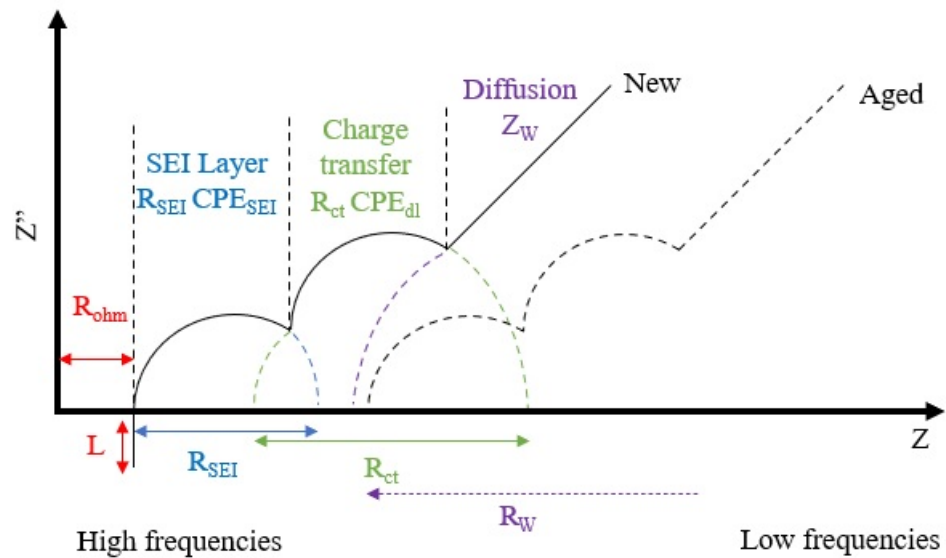


Figure 10. Idealized Nyquist plot illustrating typical impedance responses to internal lithium-ion battery phenomena based on frequency range (adapted from [166]).

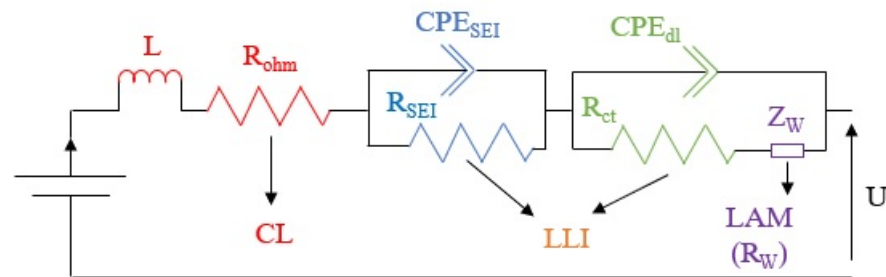


Figure 11. Equivalent circuit model illustrating the relationship between electrical elements and lithium-ion battery aging phenomena (adapted from [166]).

The ECM tracks changes of different resistances to identify and quantify cell aging mechanisms. Each resistance value is associated with a particular physical phenomenon. The ohmic resistance (R_{ohm}) represents material resistances in the battery, composed of the current collectors, connectors, and electrolyte that result in conductivity losses (CLs). The SEI resistance (R_{SEI}) represents the resistance posed by the SEI layer and implicitly, the LLI. It also hinders charge transfer reactions by reducing intercalation/de-intercalation and subsequently increases the charge transfer resistance (R_{ct}) [166]. Diffusion processes are modeled by the Warburg impedance (Z_W) defined by Equation (22):

$$Z_W = R_W \frac{\tanh\left(\left(\frac{I L^2}{D} \omega\right)^n\right)}{I \frac{L^2}{D} \omega} \tag{22}$$

The Warburg impedance is a function of the current, I , frequency, ω , specific diffusion distance, L , the effective diffusion coefficient, D , and the phase angle coefficient, n . If there are changes in the structure of the electrode, they would be captured with an increase in R_W [166].

ECM model elements are derived by fitting EIS spectra. The resistances are the horizontal distances to each depressed semicircle, where the location is indicative of the aging process occurring. Low-frequency processes such as ion diffusion are to the right of the spectra, whereas high-frequency processes such as SEI formation reactions are to the left of the spectra. Tracking the evolution of these resistances over time gives the evolution of LIB performance aging and subsequently, SOH [166].

To quantify the effects of the aging modes over cycle number, Pastor-Fernandez et al. [166] propose the growth in percentage metric, G_{EIS} , calculated for each characterization test, k , cell, i , and SOC, q , as defined by Equation (23):

$$G_{EIS} = \begin{cases} CL_{EIS,k,i}^q(\%) = \frac{R_{ohm,k,i}^q - R_{ohm,1,i}^q}{R_{ohm,1,i}^q} 100 \\ LLI_{EIS,k,i}^q(\%) = \frac{(R_{SEI,k,i}^q - R_{SEI,1,i}^q) + (R_{ct,k,i}^q - R_{ct,1,i}^q)}{R_{SEI,1,i}^q + R_{ct,1,i}^q} 100 \\ LAM_{EIS,k,i}^q(\%) = \frac{R_{W,k,i}^q - R_{W,1,i}^q}{R_{W,1,i}^q} 100 \end{cases} \quad (23)$$

EIS can also be used to extract parameters without an ECM. Al-Zubaidi et al. [167] presented a method to couple EIS and microscopy data into a finite element modelling network (FEM) to track the LIB aging.

Although EIS has promise, it is difficult to implement online in a BMS. Firstly, it requires a low-amplitude voltage or current signal for excitation, which can easily be perturbed by noise and subsequently hinder measurement accuracy. Secondly, it covers a wide range of frequencies (e.g., 2 mHz–100 kHz), which cannot be managed currently by a standard BMS controller. To remedy the frequency range problem, a separate impedance measurement system that utilizes the current signal from the DC converter for a wide range of battery excitation frequencies is typically implemented [166].

5.2.2. Incremental Capacity Differential Voltage Analysis

IC-DV analysis is conducted with a pOCV vs. charge (Q) curve. Differentiating Q with respect to pOCV derives the IC curve, whereas the opposite derives the DV curve. In an automotive application, the IC-DV curves are obtained during charging as opposed to discharging due to a more controlled, non-dynamic operation. Identification of LIB aging mechanisms from IC curves occurs with tracking peak shifts. Figure 12 provides a graphical summary for the peak shifts [166].

Any shift leading to a reduced capacity at a non-constant voltage is considered LLI, while any reduction in capacity at a constant voltage is LAM. A drop in voltage at constant capacity is considered CL [166].

To quantify aging mechanisms, a similar approach to EIS is employed with a growth in percentage metric. The formula for this parameter is presented in Equation (24) [166].

$$G_{IC-DV} = \begin{cases} CL_{IC-DV,k,i}(\%) = \frac{\max(pOCV)_{1,i} - \max(pOCV)_{k,i}}{\max(pOCV)_{1,i}} 100 \\ LLI_{IC-DV,k,i}(\%) = \frac{\text{abs}(\max(Q_1))_i - \text{abs}(\max(Q_k))_i}{\text{abs}(\max(Q_1))_i} 100 \\ LAM_{IC-DV,k,i}^q(\%) = \frac{\text{abs}\left(\left(\max\left(\frac{\Delta Q}{\Delta pOCV_1}\right)\right)_i\right) - \text{abs}\left(\max\left(\frac{\Delta Q}{\Delta pOCV_k}\right)\right)_i}{\text{abs}\left(\left(\max\left(\frac{\Delta Q}{\Delta pOCV_1}\right)\right)_i\right)} 100 \end{cases} \quad (24)$$

IC-DV analysis is less computationally expensive and model-independent as compared to EIS. However, obtaining the pOCV curve requires substantial time due to the slow charging and discharging rates needed. Additionally, unlike EIS, IC-DV quantifies aging mechanisms across the entire SOC window. Hence, the resolution of its analysis is not as fine as EIS. A potential solution is to use both mechanisms on-line in an EV for different operating conditions [166].

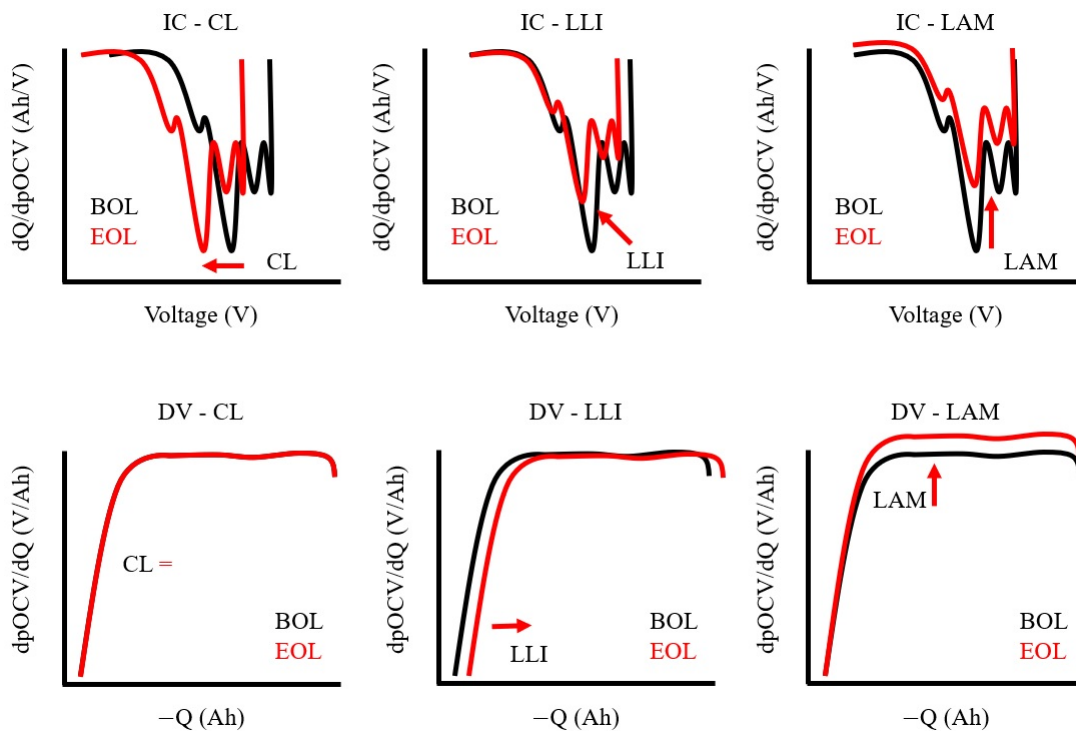


Figure 12. Incremental capacity (top), differential voltage (bottom) identification of aging mechanisms through peak shifts from the beginning to end of life (adapted from [166]).

6. Overview and Future Perspectives

This paper reviewed battery aging phenomena, aging contributing factors, and related computational models in a multiscale framework. The literature on modelling battery aging is comprehensive; however, research challenges remain, and further developments are needed.

Work on combining calendar and cycle aging is sparse. These aging modes are typically modelled separately through empirical modelling and then combined. Raj et al. [168] showed that the sequencing of aging tests influences the aging rate, especially at high C-rates. Hence, the practice of superimposing the experimental data yields an inaccurate model. Further research on combining calendar and cycle aging in a non-superimposed manner is required.

In regards to experimental testing, cell-scale testing should be temperature-controlled to mimic BTMS operation. Currently, most cell testing occurs in a thermal chamber allowing the cell's internal temperature to evolve without any control mechanism. This generates an overly conservative aging model at the cell scale which leads to prediction errors at the pack scale. Moreover, cell-spreading diagnostics should be monitored with heightened accuracy. Usually, every cell in a battery pack is not monitored by the BMS. To diagnose and subsequently validate the cell spreading phenomenon, solutions are required to improve the cell diagnostic resolution at the pack scale.

Battery modelling should also be focused on the entire battery life as opposed solely to the first life. Currently, few studies exist pertaining to modelling both the first and second life of batteries. Modelling a 20% capacity loss does not give a holistic representation of aging phenomena evolution or contributing factors at either the particle, cell, or pack scales. Thus, it is important to accurately model hierarchical LIB aging effects across the entire life cycle to increase battery reliability and thereby encourage widespread adoption.

Another area for future development is the integration of usage pattern effects (e.g., aggressiveness, external temperatures, auxiliary usage) on battery aging, since it has the potential to accelerate aging. This gives a more holistic perspective to battery aging by relating laboratory settings to real-world applications.

When validating modelling frameworks, an increased integration of post-mortem analysis techniques is required to combine all analytical data from testing with what is physically observed in a battery, and, thereby, help concretely validate the occurrence of particular aging mechanisms.

Figure 13 provides an optimized modelling and validation framework for battery aging that captures aging phenomena while being implemented in a computationally efficient manner.

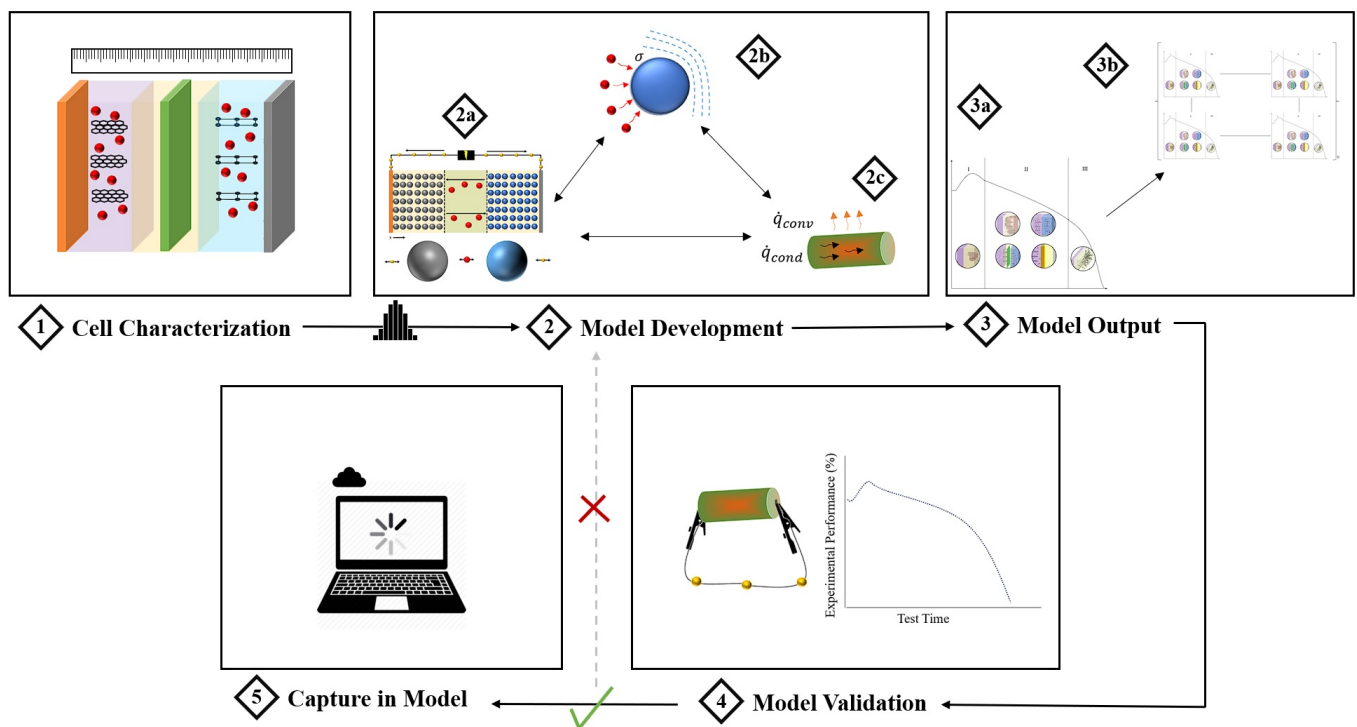


Figure 13. Proposed modelling framework: 1: cell electrochemical characterization to extract properties for model development; 2: multiple model development/coupling—2a: electrochemical model gauging cell electrical performance, 2b: mechanical model gauging particle diffusion stress and relevant cell scale effects, 2c: thermal model gauging cell temperature distribution; 3: state of health and aging mechanism composition result—3a: cell-scale results, 3b: scale up to pack-scale results using Monte Carlo distribution of parameter measurements from 1; 4: comparing model results with experimental validation (proceed to 5 if experimental correlation achieved; otherwise, retune model at 2); 5: capturing generated model framework into a machine learning interface saved in the cloud.

Simulating battery aging phenomena using a comprehensive model like the P2D enables gathering a full scope of battery operation at its limits. The proposed data-based modelling methods would efficiently model the electrochemical phenomena during aging, while generating a comprehensive battery model. When transitioning to the pack or module scale, a statistical simulation (e.g., Monte Carlo) would allow the internal battery parameters and extrinsic pack parameters to simulate the variation observed in the operating population, thereby capturing cell spreading. As battery modelling is conducted, a reduced number of experimental tests should also be implemented to test battery limits, as defined by the electrochemical model. A validation of the electrochemical model will result and enable a post-mortem analysis to effectively validate the presence of the aging mechanisms predicted. Ultimately, a combined modelling framework encompassing both multiphysics- and data-based components is considered to be the optimal choice for modelling battery aging.

Battery aging is inevitable and is a primary obstacle to the mass adoption of LIBs. However, determining aging consequences in advance of their occurrence is an effective approach to address this challenge, and must be focused on moving forward.

Author Contributions: M.A.A. was responsible for the ideation, performing the literature search and drafting all versions of this work. C.H.A. and C.M.D.S. were responsible for extensive review, editing and supervision. All authors have read and agreed to the published version of the manuscript.

Funding: This research was funded by Natural Sciences and Engineering Research Council of Canada (NSERC), MITACS, and Flex-N-Gate.

Data Availability Statement: Not applicable.

Conflicts of Interest: The authors declare no conflict of interest.

Abbreviations

The following abbreviations are used in this manuscript:

ANN	Artificial neural network
BMS	Battery Management System
BOL	Beginning of life
BTMS	Battery thermal management system
CRA	Continuous realization algorithm
CEI	Cathodic electrolyte interphase
CC-CV	Constant current - constant voltage
CNN	Convolutional neural network
DOD	Depth of discharge
DRA	Discrete realization algorithm
DST	Dynamic stress tests
ECM	Equivalent circuit model
EIS	Electrochemical impedance spectroscopy
EMD	Empirical mode decomposition
EOL	End of life
EV	Electric vehicles
FFLSRA	Forgetting factor recursive least squares algorithm
FUDS	Federal urban driving schedules
GM	General Motors
HRA	Hybrid realization algorithm
IC-DV	Incremental capacity/differential voltage
ISPM+	Improved SPM
KRR	Kernel ridge regression
LAM	Loss of active material
LRA	Lagrange interpolation realization algorithm
LCO	Lithium Cobalt Oxide
LIB	Lithium-ion battery
LLI	Loss of lithium inventory
LFP	Lithium Iron Phosphate
LMO	Lithium Manganese Oxide
LSTM	Long short term memory
LTO	Lithium Titante Oxide
NCA	Nickel Cobalt Aluminum Oxide
NEDC	New european driving cycle
NMC	Nickel Manganese Cobalt Oxide
OCV	Open circuit voltage
OEM	Original equipment manufacturer
P2D	Pseudo 2D model

PCM	Phase change material
PDE	Partial differential equation
PHEV	Plug in hybrid electric vehicle
pOCV	Pseudo OCV
RDE	Remaining discharge energy
RMSE	Root mean squared error
RNN	Recurrent neural network
ROM	Reduced order model
RPT	Reference performance test
SEI	Solid electrolyte interphase
SPM	Single particle model
SOC	State of charge
SOH	State of health
SVM	Support vector machine
TEMA	Transport technology and mobility
V2G	Vehicle to grid
WLTP	World harmonized light duty vehicle test procedures

References

- Blomgren, G.E. The Development and Future of Lithium Ion Batteries. *J. Electrochem. Soc.* **2017**, *164*, A5019–A5025. [CrossRef]
- Xiong, R.; Pan, Y.; Shen, W.; Li, H.; Sun, F. Lithium-ion battery aging mechanisms and diagnosis method for automotive applications: Recent advances and perspectives. *Renew. Sustain. Energy Rev.* **2020**, *131*, 110048. [CrossRef]
- Riley, C. The great electric car race is just beginning. *CNN Business*. Available online: <https://www.cnn.com/interactive/2019/08/business/electric-cars-audi-volkswagen-tesla/> (accessed on 15 December 2021).
- Zhao, Y.; Patel, Y.; Zhang, T.; Offer, G.J. Modeling the Effects of Thermal Gradients Induced by Tab and Surface Cooling on Lithium Ion Cell Performance. *J. Electrochem. Soc.* **2018**, *165*, A3169–A3178. [CrossRef]
- Han, X.; Lu, L.; Zheng, Y.; Feng, X.; Li, Z.; Li, J.; Ouyang, M. A review on the key issues of the lithium ion battery degradation among the whole life cycle. *eTransportation* **2019**, *1*, 100005. [CrossRef]
- Keil, P.; Schuster, S.F.; Wilhelm, J.; Travi, J.; Hauser, A.; Karl, R.C.; Jossen, A. Calendar Aging of Lithium-Ion Batteries. *J. Electrochem. Soc.* **2016**, *163*, A1872–A1880. [CrossRef]
- Galatro, D.; Romero, D.A.; Freitez, J.A.; Da Silva, C.; Trescases, O.; Amon, C.H. Modeling degradation of lithium-ion batteries considering cell-to-cell variations. *J. Energy Storage* **2021**, *44*, 103478. [CrossRef]
- Wu, B.; Widanage, W.D.; Yang, S.; Liu, X. Battery digital twins: Perspectives on the fusion of models, data and artificial intelligence for smart battery management systems. *Energy AI* **2020**, *1*, 100016. [CrossRef]
- Ma, S.; Jiang, M.; Tao, P.; Song, C.; Wu, J.; Wang, J.; Deng, T.; Shang, W. Temperature effect and thermal impact in lithium-ion batteries: A review. *Prog. Nat. Sci. Mater. Int.* **2018**, *28*, 653–666. [CrossRef]
- Zhang, X.; Soc, J.E.; Zhang, X.; Sastry, A.M.; Shyy, W. Intercalation-Induced Stress and Heat Generation within Single Lithium-Ion Battery Cathode Particles Intercalation-Induced Stress and Heat Generation within Single Lithium-Ion Battery Cathode Particles. *J. Electrochem. Soc.* **2008**, *155*, A542–A552. [CrossRef]
- Galatro, D.; Al-Zareer, M.; Da Silva, C.; Romero, D.A.; Amon, C.H. Thermal behavior of Lithium-ion batteries: Aging, heat generation, thermal management and failure. *Front. Heat Mass Transf.* **2020**, *14*, 1–18. [CrossRef]
- Feng, F.; Hu, X.; Hu, L.; Hu, F.; Li, Y.; Zhang, L. Propagation mechanisms and diagnosis of parameter inconsistency within Li-Ion battery packs. *Renew. Sustain. Energy Rev.* **2019**, *112*, 102–113. [CrossRef]
- Kang, D.; Lee, P.Y.; Yoo, K.; Kim, J. Internal thermal network model-based inner temperature distribution of high-power lithium-ion battery packs with different shapes for thermal management. *J. Energy Storage* **2020**, *27*, 101017. [CrossRef]
- Atalay, S.; Sheikh, M.; Mariani, A.; Merla, Y.; Bower, E.; Widanage, W.D. Theory of battery ageing in a lithium-ion battery: Capacity fade, nonlinear ageing and lifetime prediction. *J. Power Sources* **2020**, *478*, 229026. [CrossRef]
- Qi, Y.; Harris, S.J. In Situ Observation of Strains during Lithiation of a Graphite Electrode. *J. Electrochem. Soc.* **2010**, *157*, A741–A747. [CrossRef]
- Xu, Y.; Hu, E.; Zhang, K.; Wang, X.; Borzenets, V.; Sun, Z.; Pianetta, P.; Yu, X.; Liu, Y.; Yang, X.Q.; et al. In situ Visualization of State-of-Charge Heterogeneity within a LiCoO₂ Particle that Evolves upon Cycling at Different Rates. *ACS Energy Lett.* **2017**, *2*, 1240–1245. [CrossRef]
- Xu, R.; Sun, H.; de Vasconcelos, L.S.; Zhao, K. Mechanical and Structural Degradation of LiNi_xMn_yCo_zO₂ Cathode in Li-Ion Batteries: An Experimental Study. *J. Electrochem. Soc.* **2017**, *164*, A3333–A3341. [CrossRef]
- Trevisanello, E.; Ruess, R.; Conforto, G.; Richter, F.H.; Janek, J. Polycrystalline and Single Crystalline NCM Cathode Materials—Quantifying Particle Cracking, Active Surface Area, and Lithium Diffusion. *Adv. Energy Mater.* **2021**, *11*, 2003400. [CrossRef]
- Lee, Y.K.; Park, J.; Lu, W. A Comprehensive Experimental and Modeling Study on Dissolution in Li-Ion Batteries. *J. Electrochem. Soc.* **2019**, *166*, A1340–A1354. [CrossRef]

20. Zhuo, M.; Offer, G.; Marinescu, M. Degradation model of high-nickel positive electrodes: Effects of loss of active material and cyclable lithium on capacity fade. *J. Power Sources* **2023**, *556*, 232461. [[CrossRef](#)]
21. Kim, D.H.; Song, J.H.; Jung, C.H.; Eum, D.; Kim, B.; Hong, S.H.; Kang, K. Stepwise Dopant Selection Process for High-Nickel Layered Oxide Cathodes. *Adv. Energy Mater.* **2022**, *12*, 2200136. [[CrossRef](#)]
22. Bank, T.; Feldmann, J.; Klamor, S.; Bihn, S.; Sauer, D.U. Extensive aging analysis of high-power lithium titanate oxide batteries: Impact of the passive electrode effect. *J. Power Sources* **2020**, *473*, 228566. [[CrossRef](#)]
23. Logan, E.R.; Hebecker, H.; Eldesoky, A.; Luscombe, A.; Johnson, M.B.; Dahn, J.R. Performance and Degradation of LiFePO₄/Graphite Cells: The Impact of Water Contamination and an Evaluation of Common Electrolyte Additives. *J. Electrochem. Soc.* **2020**, *167*, 130543. [[CrossRef](#)]
24. Werner, D.; Paarmann, S.; Wetzel, T. Calendar aging of li-ion cells—Experimental investigation and empirical correlation. *Batteries* **2021**, *7*, 28. [[CrossRef](#)]
25. Schmitt, J.; Maheshwari, A.; Heck, M.; Lux, S.; Vetter, M. Impedance change and capacity fade of lithium nickel manganese cobalt oxide-based batteries during calendar aging. *J. Power Sources* **2017**, *353*, 183–194. [[CrossRef](#)]
26. Sieg, J.; Schmid, A.U.; Rau, L.; Gesterkamp, A.; Storch, M.; Spier, B.; Birke, K.P.; Sauer, D.U. Fast-charging capability of lithium-ion cells: Influence of electrode aging and electrolyte consumption. *Appl. Energy* **2022**, *305*, 117747. [[CrossRef](#)]
27. Rechhammer, S.K.; Zang, X.; Zhang, W.; Sawodny, O. Calendar and cycle aging study of a commercial LiMn₂O₄ cell under consideration of influences by cell progress. *J. Energy Storage* **2020**, *30*, 101547. [[CrossRef](#)]
28. Chahbaz, A.; Meishner, F.; Li, W.; Ünlübayir, C.; Uwe Sauer, D. Non-invasive identification of calendar and cyclic ageing mechanisms for lithium-titanate-oxide batteries. *Energy Storage Mater.* **2021**, *42*, 794–805. [[CrossRef](#)]
29. Zhao, Y.; Stein, P.; Bai, Y.; Al-Siraj, M.; Yang, Y.; Xu, B.X. A review on modeling of electro-chemo-mechanics in lithium-ion batteries. *J. Power Sources* **2019**, *413*, 259–283. [[CrossRef](#)]
30. Yang, X.G.; Leng, Y.; Zhang, G.; Ge, S.; Wang, C.Y. Modeling of lithium plating induced aging of lithium-ion batteries: Transition from linear to nonlinear aging. *J. Power Sources* **2017**, *360*, 28–40. [[CrossRef](#)]
31. Liu, J.; Duan, Q.; Ma, M.; Zhao, C.; Sun, J.; Wang, Q. Aging mechanisms and thermal stability of aged commercial 18650 lithium ion battery induced by slight overcharging cycling. *J. Power Sources* **2020**, *445*, 227263. [[CrossRef](#)]
32. Jaguemont, J.; Boulon, L.; Dubé, Y. A comprehensive review of lithium-ion batteries used in hybrid and electric vehicles at cold temperatures. *Appl. Energy* **2016**, *164*, 99–114. [[CrossRef](#)]
33. Jaguemont, J.; Boulon, L.; Venet, P.; Dube, Y.; Sari, A. Lithium-Ion Battery Aging Experiments at Subzero Temperatures and Model Development for Capacity Fade Estimation. *IEEE Trans. Veh. Technol.* **2016**, *65*, 4328–4343. [[CrossRef](#)]
34. Gao, T.; Bai, J.; Ouyang, D.; Wang, Z.; Bai, W.; Mao, N.; Zhu, Y. Effect of aging temperature on thermal stability of lithium-ion batteries: Part A – High-temperature aging. *Renew. Energy* **2023**, *203*, 592–600. [[CrossRef](#)]
35. Spotte-Smith, E.W.C.; Petrocelli, T.B.; Patel, H.D.; Blau, S.M.; Persson, K.A. Elementary Decomposition Mechanisms of Lithium Hexafluorophosphate in Battery Electrolytes and Interphases. *Acs Energy Lett.* **2023**, *8*, 347–355. [[CrossRef](#)]
36. Zhu, J.; Dewi Darma, M.S.; Knapp, M.; Sørensen, D.R.; Heere, M.; Fang, Q.; Wang, X.; Dai, H.; Mereacre, L.; Senyshyn, A.; et al. Investigation of lithium-ion battery degradation mechanisms by combining differential voltage analysis and alternating current impedance. *J. Power Sources* **2020**, *448*, 28–30. [[CrossRef](#)]
37. Leonardi, S.G.; Aloisio, D.; Brunaccini, G.; Stassi, A.; Ferraro, M.; Antonucci, V.; Sergi, F. Investigation on the ageing mechanism for a lithium-ion cell under accelerated tests: The case of primary frequency regulation service. *J. Energy Storage* **2021**, *41*, 102904. [[CrossRef](#)]
38. Ryu, H.H.; Park, K.J.; Yoon, C.S.; Sun, Y.K. Capacity fading of ni-rich li[Ni_xCo_yMn_{1-x-y}]O₂ (0.6 ≤ x ≤ 0.95) Cathodes for High-Energy-Density Lithium-Ion Batteries: Bulk or Surface Degradation? *Chem. Mater.* **2018**, *30*, 1155–1163. [[CrossRef](#)]
39. Preger, Y.; Barkholtz, H.M.; Fresquez, A.; Campbell, D.L.; Juba, B.W.; Romàn-Kustas, J.; Ferreira, S.R.; Chalamala, B. Degradation of Commercial Lithium-Ion Cells as a Function of Chemistry and Cycling Conditions. *J. Electrochem. Soc.* **2020**, *167*, 120532. [[CrossRef](#)]
40. Martinez-Laserna, E.; Sarasketa-Zabala, E.; Villarreal Sarria, I.; Stroe, D.I.; Swierczynski, M.; Warnecke, A.; Timmermans, J.M.; Goutam, S.; Omar, N.; Rodriguez, P. Technical Viability of Battery Second Life: A Study from the Ageing Perspective. *IEEE Trans. Ind. Appl.* **2018**, *54*, 2703–2713. [[CrossRef](#)]
41. Braco, E.; San Martín, I.; Berrueta, A.; Sanchis, P.; Ursúa, A. Experimental assessment of cycling ageing of lithium-ion second-life batteries from electric vehicles. *J. Energy Storage* **2020**, *32*, 101695. [[CrossRef](#)]
42. Casals, L.C.; García, B.A.; Aguesse, F.; Iturrondobeitia, A. Second life of electric vehicle batteries: Relation between materials degradation and environmental impact. *Int. J. Life Cycle Assess.* **2017**, *22*, 82–93. [[CrossRef](#)]
43. Zheng, Y.; Ouyang, M.; Lu, L.; Li, J. Understanding aging mechanisms in lithium-ion battery packs: From cell capacity loss to pack capacity evolution. *J. Power Sources* **2015**, *278*, 287–295. [[CrossRef](#)]
44. Zilberman, I.; Schmitt, J.; Ludwig, S.; Naumann, M.; Jossen, A. Simulation of voltage imbalance in large lithium-ion battery packs influenced by cell-to-cell variations and balancing systems. *J. Energy Storage* **2020**, *32*, 101828. [[CrossRef](#)]
45. Wang, X.; Wang, Z.; Wang, L.; Wang, Z.; Guo, H. Dependency analysis and degradation process-dependent modeling of lithium-ion battery packs. *J. Power Sources* **2019**, *414*, 318–326. [[CrossRef](#)]
46. Yuksel, T.; Litster, S.; Viswanathan, V.; Michalek, J.J. Plug-in hybrid electric vehicle LiFePO₄ battery life implications of thermal management, driving conditions, and regional climate. *J. Power Sources* **2017**, *338*, 49–64. [[CrossRef](#)]

47. Keil, P.; Jossen, A. Aging of Lithium-Ion Batteries in Electric Vehicles: Impact of Regenerative Braking EVS28 International Electric Vehicle Symposium and Exhibition 2. *World Electr. Veh. J.* **2015**, *7*, 41–51. [[CrossRef](#)]
48. Mueller, S.; Rohr, S.; Schmid, W.; Lienkamp, M. Analysing the influence of driver behaviour and tuning measures on battery aging and residual value of electric vehicles. In Proceedings of the EVS 2017—30th International Electric Vehicle Symposium and Exhibition, Stuttgart, Germany, 9–11 October 2017; pp. 1–12.
49. Liu, H.; Chen, F.; Tong, Y.; Wang, Z.; Yu, X.; Huang, R. Impacts of driving conditions on ev battery pack life cycle. *World Electr. Veh. J.* **2020**, *11*, 17. [[CrossRef](#)]
50. Jafari, M.; Gauchia, A.; Zhao, S.; Zhang, K.; Gauchia, L. Electric Vehicle Battery Cycle Aging Evaluation in Real-World Daily Driving and Vehicle-to-Grid Services. *IEEE Trans. Transp. Electrification* **2017**, *4*, 122–134. [[CrossRef](#)]
51. Xia, Q.; Wang, Z.; Ren, Y.; Tao, L.; Lu, C.; Tian, J.; Hu, D.; Wang, Y.; Su, Y.; Chong, J.; et al. A modified reliability model for lithium-ion battery packs based on the stochastic capacity degradation and dynamic response impedance. *J. Power Sources* **2019**, *423*, 40–51. [[CrossRef](#)]
52. Maheshwari, A.; Paterakis, N.G.; Santarelli, M.; Gibescu, M. Optimizing the operation of energy storage using a non-linear lithium-ion battery degradation model. *Appl. Energy* **2020**, *261*, 114360. [[CrossRef](#)]
53. Suri, G.; Onori, S. A control-oriented cycle-life model for hybrid electric vehicle lithium-ion batteries. *Energy* **2016**, *96*, 644–653. [[CrossRef](#)]
54. De Gennaro, M.; Paffumi, E.; Martini, G.; Giallonardo, A.; Pedroso, S.; Loiseau-Lapointe, A. A case study to predict the capacity fade of the battery of electrified vehicles in real-world use conditions. *Case Stud. Transp. Policy* **2020**, *8*, 517–534. [[CrossRef](#)]
55. Xu, B.; Oudalov, A.; Ulbig, A.; Andersson, G.; Kirschen, D.S. Modeling of lithium-ion battery degradation for cell life assessment. *IEEE Trans. Smart Grid* **2018**, *9*, 1131–1140. [[CrossRef](#)]
56. Redondo-Iglesias, E.; Venet, P.; Pelissier, S. Modelling lithium-ion battery ageing in electric vehicle applications—calendar and cycling ageing combination effects. *Batteries* **2020**, *6*, 14. [[CrossRef](#)]
57. Galatro, D.; Silva, C.D.; Romero, D.A.; Trescases, O.; Amon, C.H. Challenges in data-based degradation models for lithium-ion batteries. *Int. J. Energy Res.* **2020**, *44*, 3954–3975. [[CrossRef](#)]
58. Zhang, S.; Hu, X.; Xie, S.; Song, Z.; Hu, L.; Hou, C. Adaptively coordinated optimization of battery aging and energy management in plug-in hybrid electric buses. *Appl. Energy* **2019**, *256*, 113891. [[CrossRef](#)]
59. Du, R.; Hu, X.; Xie, S.; Hu, L.; Zhang, Z.; Lin, X. Battery aging- and temperature-aware predictive energy management for hybrid electric vehicles. *J. Power Sources* **2020**, *473*, 228568. [[CrossRef](#)]
60. Nikolian, A.; Jaguemont, J.; de Hoog, J.; Goutam, S.; Omar, N.; Van Den Bossche, P.; Van Mierlo, J. Complete cell-level lithium-ion electrical ECM model for different chemistries (NMC, LFP, LTO) and temperatures (−5 °C to 45 °C)—Optimized modelling techniques. *Int. J. Electr. Power Energy Syst.* **2018**, *98*, 133–146. [[CrossRef](#)]
61. Su, J.; Lin, M.; Wang, S.; Li, J.; Coffie-Ken, J.; Xie, F. An equivalent circuit model analysis for the lithium-ion battery pack in pure electric vehicles. *Meas. Control* **2019**, *52*, 193–201. [[CrossRef](#)]
62. Ding, X.; Zhang, D.; Cheng, J.; Wang, B.; Luk, P.C.K. An improved Thevenin model of lithium-ion battery with high accuracy for electric vehicles. *Appl. Energy* **2019**, *254*, 113615. [[CrossRef](#)]
63. Hosseinzadeh, E.; Arias, S.; Krishna, M.; Worwood, D.; Barai, A.; Widanalage, D.; Marco, J. Quantifying cell-to-cell variations of a parallel battery module for different pack configurations. *Appl. Energy* **2021**, *282*, 115859. [[CrossRef](#)]
64. Escobar, C.; Gong, Z.; Da Silva, C.; Trescases, O.; Amon, C.H. Effect of Cell-to-Cell Thermal Imbalance and Cooling Strategy on Electric Vehicle Battery Performance and Longevity. In Proceedings of the 2022 21st IEEE Intersociety Conference on Thermal and Thermomechanical Phenomena in Electronic Systems (iTherm), San Diego, CA, USA, 31 May–1 June 2022; pp. 1–9. [[CrossRef](#)]
65. Mao, Y.; Wang, X.; Xia, S.; Zhang, K.; Wei, C.; Bak, S.; Shadik, Z.; Liu, X.; Yang, Y.; Xu, R.; et al. High-Voltage Charging-Induced Strain, Heterogeneity, and Micro-Cracks in Secondary Particles of a Nickel-Rich Layered Cathode Material. *Adv. Funct. Mater.* **2019**, *1900247*, 1–11. [[CrossRef](#)]
66. Liu, B.; Yang, J.; Yang, H.; Ye, C.; Mao, Y.; Wang, J.; Shi, S.; Yang, J.; Zhang, W. Rationalizing the interphase stability of Li_{1-x} doped-Li₇La₃Zr₂O₁₂ via automated reaction screening and machine learning. *J. Mater. Chem.* **2019**, *12*, 19961–19969. [[CrossRef](#)]
67. Roman, D.; Saxena, S.; Robu, V.; Pecht, M.; Flynn, D. Machine learning pipeline for battery state-of-health estimation. *Nat. Mach. Intell.* **2021**, *3*, 447–456. [[CrossRef](#)]
68. Li, Y.; Zou, C.; Berecibar, M.; Nanini-Maury, E.; Chan, J.C.; van den Bossche, P.; Van Mierlo, J.; Omar, N. Random forest regression for online capacity estimation of lithium-ion batteries. *Appl. Energy* **2018**, *232*, 197–210. [[CrossRef](#)]
69. Zhang, Y.; Tang, Q.; Zhang, Y.; Wang, J.; Stimming, U.; Lee, A.A. Identifying degradation patterns of lithium ion batteries from impedance spectroscopy using machine learning. *Nat. Commun.* **2020**, *11*, 6–11. [[CrossRef](#)] [[PubMed](#)]
70. Son, S.; Jeong, S.; Kwak, E.; Kim, J.-h.; Oh, K.Y. Integrated framework for SOH estimation of lithium-ion batteries using multiphysics features. *Energy* **2022**, *238*, 121712. [[CrossRef](#)]
71. Li, H.; Ji, W.; Zhang, P.; Zhao, J. Safety boundary of power battery based on quantitative lithium deposition. *J. Energy Storage* **2022**, *52*, 104789. [[CrossRef](#)]
72. Chen, B.R.; Kunz, M.R.; Tanim, T.R.; Dufek, E.J. A machine learning framework for early detection of lithium plating combining multiple physics-based electrochemical signatures. *Cell Rep. Phys. Sci.* **2021**, *2*, 100352. [[CrossRef](#)]

73. Liu, D.; Zhou, J.; Pan, D.; Peng, Y.; Peng, X. Lithium-ion battery remaining useful life estimation with an optimized Relevance Vector Machine algorithm with incremental learning. *Meas. J. Int. Meas. Confed.* **2015**, *63*. [[CrossRef](#)]
74. Ni, Y.; Xu, J.; Zhu, C.; Pei, L. Accurate residual capacity estimation of retired LiFePO₄ batteries based on mechanism and data-driven model. *Appl. Energy* **2022**, *305*, 117922. [[CrossRef](#)]
75. Johnen, M.; Pitzten, S.; Kamps, U.; Kateri, M.; Dechent, P.; Sauer, D.U. Modeling long-term capacity degradation of lithium-ion batteries. *J. Energy Storage* **2021**, *34*, 102011. [[CrossRef](#)]
76. Weng, C.; Feng, X.; Sun, J.; Peng, H. State-of-health monitoring of lithium-ion battery modules and packs via incremental capacity peak tracking. *Appl. Energy* **2016**, *180*, 360–368. [[CrossRef](#)]
77. Zhou, Y.; Huang, M.; Pecht, M. Remaining useful life estimation of lithium-ion cells based on k-nearest neighbor regression with differential evolution optimization. *J. Clean. Prod.* **2020**, *249*, 119409. [[CrossRef](#)]
78. Deng, Z.; Hu, X.; Lin, X.; Che, Y.; Xu, L.; Guo, W. Data-driven state of charge estimation for lithium-ion battery packs based on Gaussian process regression. *Energy* **2020**, *205*, 118000. [[CrossRef](#)]
79. Severson, K.A.; Attia, P.M.; Jin, N.; Perkins, N.; Jiang, B.; Yang, Z.; Chen, M.H.; Aykol, M.; Herring, P.K.; Fraggedakis, D.; et al. Data-driven prediction of battery cycle life before capacity degradation. *Nat. Energy* **2019**, *4*, 383–391. [[CrossRef](#)]
80. Fei, Z.; Yang, F.; Tsui, K.L.; Li, L.; Zhang, Z. Early prediction of battery lifetime via a machine learning based framework. *Energy* **2021**, *225*, 120205. [[CrossRef](#)]
81. Kong, J.-z.; Yang, F.; Zhang, X.; Pan, E.; Peng, Z.; Wang, D. Voltage-temperature health feature extraction to improve prognostics and health management of lithium-ion batteries. *Energy* **2021**, *223*, 120114. [[CrossRef](#)]
82. Diao, W.; Naqvi, I.H.; Pecht, M. Early detection of anomalous degradation behavior in lithium-ion batteries. *J. Energy Storage* **2020**, *32*, 101710. [[CrossRef](#)]
83. Lee, S.; Kim, Y. Li-ion Battery Electrode Health Diagnostics using Machine Learning. In Proceedings of the American Control Conference, Denver, CO, USA, 1–3 July 2020; pp. 1137–1142. [[CrossRef](#)]
84. Qian, G.; Zhang, J.; Chu, S.q.; Li, J.; Zhang, K.; Yuan, Q.; Pianetta, P.; Li, L.; Jung, K.; Liu, Y. Understanding the Mesoscale Degradation in Nickel-Rich Cathode Materials through Machine-Learning-Revealed Strain—Redox Decoupling. *ACS Energy Lett.* **2021**, *6*, 687–693. [[CrossRef](#)]
85. Jiang, Z.; Li, J.; Yang, Y.; Mu, L.; Wei, C.; Yu, X.; Zhao, K.; Cloetens, P.; Lin, F.; Liu, Y.; et al. Machine-learning-revealed statistics of the particle-carbon/binder detachment in lithium-ion battery cathodes. *Nat. Commun.* **2020**, *11*, 2310. [[CrossRef](#)]
86. Bhowmik, A.; Castelli, I.E.; Garcia-lastra, J.M.; Bj, P.; Winther, O.; Vegge, T. A perspective on inverse design of battery interphases using multi-scale modelling, experiments and generative deep learning. *Energy Storage Mater.* **2019**, *21*, 446–456. [[CrossRef](#)]
87. Lee, S.; Han, S.; Han, K.H.; Kim, Y.; Agarwal, S.; Hariharan, K.S.; Oh, B.; Yoon, J. Diagnosing various failures of lithium-ion batteries using artificial neural network enhanced by likelihood mapping. *J. Energy Storage* **2021**, *40*, 102768. [[CrossRef](#)]
88. Ruan, H.; Chen, J.; Ai, W.; Wu, B. Generalised diagnostic framework for rapid battery degradation quantification with deep learning. *Energy AI* **2022**, *9*, 100158. [[CrossRef](#)]
89. Chun, H.; Yoon, K.; Kim, J.; Han, S. Improving aging identifiability of lithium-ion batteries using deep reinforcement learning. *IEEE Trans. Transp. Electrif.* **2022**, *9*, 995–1007. [[CrossRef](#)]
90. Zhang, Y.; Xiong, R.; He, H.; Pecht, M.G. Long short-term memory recurrent neural network for remaining useful life prediction of lithium-ion batteries. *IEEE Trans. Veh. Technol.* **2018**, *67*, 5695–5705. [[CrossRef](#)]
91. Assefi, M.; Hooshmand, A.; Hosseini, H.; Sharma, R. Battery Degradation Temporal Modeling Using LSTM Networks. In Proceedings of the 17th IEEE International Conference on Machine Learning and Applications, ICMLA 2018, Orlando, FL, USA, 17–20 December 2019; pp. 853–858. [[CrossRef](#)]
92. Liu, K.; Shang, Y.; Ouyang, Q.; Widanage, W.D. A Data-Driven Approach with Uncertainty Quantification for Predicting Future Capacities and Remaining Useful Life of Lithium-ion Battery. *IEEE Trans. Ind. Electron.* **2021**, *68*, 3170–3180. [[CrossRef](#)]
93. Azkue, M.; Lucu, M.; Martinez-Laserna, E.; Aizpuru, I. Calendar ageing model for Li-Ion batteries using transfer learning methods. *World Electr. Veh. J.* **2021**, *12*, 145. [[CrossRef](#)]
94. Tang, X.; Liu, K.; Wang, X.; Gao, F.; MacRo, J.; Widanage, W.D. Model Migration Neural Network for Predicting Battery Aging Trajectories. *IEEE Trans. Transp. Electrif.* **2020**, *6*, 363–374. [[CrossRef](#)]
95. Takyi-Aninakwa, P.; Wang, S.; Zhang, H.; Li, H.; Xu, W.; Fernandez, C. An optimized relevant long short-term memory-squared gain extended Kalman filter for the state of charge estimation of lithium-ion batteries. *Energy* **2022**, *260*, 125093. [[CrossRef](#)]
96. Song, L.; Zhang, K.; Liang, T.; Han, X.; Zhang, Y. Intelligent state of health estimation for lithium-ion battery pack based on big data analysis. *J. Energy Storage* **2020**, *32*, 101836. [[CrossRef](#)]
97. Che, Y.; Deng, Z.; Li, P.; Tang, X.; Khosravinia, K.; Lin, X.; Hu, X. State of health prognostics for series battery packs: A universal deep learning method. *Energy* **2022**, *238*, 121857. [[CrossRef](#)]
98. Shu, X.; Shen, J.; Li, G.; Zhang, Y.; Chen, Z.; Liu, Y. A Flexible State-of-Health Prediction Scheme for Lithium-Ion Battery Packs with Long Short-Term Memory Network and Transfer Learning. *IEEE Trans. Transp. Electrif.* **2021**, *7*, 2238–2248. [[CrossRef](#)]
99. Shen, S.; Sadoughi, M.; Chen, X.; Hong, M.; Hu, C. A deep learning method for online capacity estimation of lithium-ion batteries. *J. Energy Storage* **2019**, *25*, 100817. [[CrossRef](#)]
100. Khaleghi, S.; Karimi, D.; Beheshti, S.H.; Hosen, M.S.; Behi, H.; Bereibar, M.; Van Mierlo, J. Online health diagnosis of lithium-ion batteries based on nonlinear autoregressive neural network. *Appl. Energy* **2021**, *282*, 116159. [[CrossRef](#)]

101. Smiley, A.J.; Harrison, W.K.; Plett, G.L. Postprocessing the outputs of an interacting multiple-model Kalman filter using a Markovian trellis to estimate parameter values of aged Li-ion cells. *J. Energy Storage* **2020**, *27*, 101043. [[CrossRef](#)]
102. Xu, Z.; Wang, J.; Fan, Q.; Lund, P.D.; Hong, J. Improving the state of charge estimation of reused lithium-ion batteries by abating hysteresis using machine learning technique. *J. Energy Storage* **2020**, *32*, 101678. [[CrossRef](#)]
103. Yang, C.; Wang, X.; Fang, Q.; Dai, H.; Cao, Y.; Wei, X. An online SOC and capacity estimation method for aged lithium-ion battery pack considering cell inconsistency. *J. Energy Storage* **2020**, *29*, 101250. [[CrossRef](#)]
104. Tang, X.; Liu, K.; Wang, X.; Liu, B.; Gao, F.; Widanage, W.D. Real-time aging trajectory prediction using a base model-oriented gradient-correction particle filter for Lithium-ion batteries. *J. Power Sources* **2019**, *440*, 227118. [[CrossRef](#)]
105. Meng, J.; Azib, T.; Yue, M. Early-Stage end-of-Life prediction of lithium-Ion battery using empirical mode decomposition and particle filter. *Proc. Inst. Mech. Eng. Part J. Power Energy* **2023**, *237*, 1090–1099. [[CrossRef](#)]
106. Kannan, V.; Fisher, A.; Birgersson, E. Monte Carlo assisted sensitivity analysis of a Li-ion battery with a phase change material. *J. Energy Storage* **2021**, *35*, 102269. [[CrossRef](#)]
107. Rogers, D.J.; Aslett, L.J.; Troffaes, M.C. Modelling of modular battery systems under cell capacity variation and degradation. *Appl. Energy* **2021**, *283*, 116360. [[CrossRef](#)]
108. Lin, Y.C.; Chung, K.J. Lifetime prognosis of lithium-ion batteries through novel accelerated degradation measurements and a combined gamma process and Monte Carlo method. *Appl. Sci.* **2019**, *9*, 559. [[CrossRef](#)]
109. Wang, L.; Sun, Y.; Wang, X.; Wang, Z.; Zhao, X. Reliability modeling method for lithium-ion battery packs considering the dependency of cell degradations based on a regression model and copulas. *Materials* **2019**, *12*, 1054. [[CrossRef](#)]
110. Lai, X.; Huang, Y.; Gu, H.; Han, X.; Feng, X.; Dai, H.; Zheng, Y.; Ouyang, M. Remaining discharge energy estimation for lithium-ion batteries based on future load prediction considering temperature and ageing effects. *Energy* **2022**, *238*, 121754. [[CrossRef](#)]
111. Duan, B.; Li, Z.; Gu, P.; Zhou, Z.; Zhang, C. Evaluation of battery inconsistency based on information entropy. *J. Energy Storage* **2018**, *16*, 160–166. [[CrossRef](#)]
112. Doyle, M.; Fuller, T.F.; Newman, J. Modeling of Galvanostatic Charge and Discharge of the Lithium/Polymer/Insertion Cell. *J. Electrochem. Soc.* **1993**, *140*, 1526. [[CrossRef](#)]
113. Abada, S.; Marlair, G.; Lecocq, A.; Petit, M.; Sauvant-Moynot, V.; Huet, F. Safety focused modeling of lithium-ion batteries: A review. *J. Power Sources* **2016**, *306*, 178–192. [[CrossRef](#)]
114. Torchio, M.; Magni, L.; Gopaluni, R.B.; Braatz, R.D.; Raimondo, D.M. LIONSIMBA: A Matlab Framework Based on a Finite Volume Model Suitable for Li-Ion Battery Design, Simulation, and Control. *J. Electrochem. Soc.* **2016**, *163*, A1192–A1205. [[CrossRef](#)]
115. Li, J.; Wang, D.; Deng, L.; Cui, Z.; Lyu, C.; Wang, L.; Pecht, M. Aging modes analysis and physical parameter identification based on a simplified electrochemical model for lithium-ion batteries. *J. Energy Storage* **2020**, *31*, 101538. [[CrossRef](#)]
116. Jokar, A.; Rajabloo, B.; Désilets, M.; Lacroix, M. Review of simplified Pseudo-two-Dimensional models of lithium-ion batteries. *J. Power Sources* **2016**, *327*, 44–55. [[CrossRef](#)]
117. Dao, T.S.; Vyasrayani, C.P.; McPhee, J. Simplification and order reduction of lithium-ion battery model based on porous-electrode theory. *J. Power Sources* **2012**, *198*, 329–337. [[CrossRef](#)]
118. Smiley, A.; Plett, G.L. An adaptive physics-based reduced-order model of an aged lithium-ion cell, selected using an interacting multiple-model Kalman filter. *J. Energy Storage* **2018**, *19*, 120–134. [[CrossRef](#)]
119. Lv, H.; Huang, X.; Kang, L.; Liu, Y. Quantitative Estimation of Turning Point of Ageing Based on a Two-Stage Model for Lithium-Ion Batteries. *J. Electrochem. Soc.* **2022**, *169*, 010533. [[CrossRef](#)]
120. Chen, Z.; Danilov, D.L.; Zhang, Q.; Jiang, M.; Zhou, J.; Eichel, R.A.; Notten, P.H. Modeling NCA/C6-Si battery ageing. *Electrochim. Acta* **2022**, *430*, 141077. [[CrossRef](#)]
121. Carelli, S.; Bessler, W.G. Coupling Lithium Plating with SEI Formation in a Pseudo-3D Model: A Comprehensive Approach to Describe Aging in Lithium-Ion Cells. *J. Electrochem. Soc.* **2022**, *169*, 050539. [[CrossRef](#)]
122. O’Kane, S.E.; Ai, W.; Madabattula, G.; Alonso-Alvarez, D.; Timms, R.; Sulzer, V.; Edge, J.S.; Wu, B.; Offer, G.J.; Marinescu, M. Lithium-ion battery degradation: How to model it. *Phys. Chem. Chem. Phys.* **2022**, *24*, 7909–7922. [[CrossRef](#)]
123. Ashwin, T.R.; McGordon, A.; Jennings, P.A. Electrochemical modelling of Li-ion battery pack with constant voltage cycling. *J. Power Sources* **2017**, *341*, 327–339. [[CrossRef](#)]
124. Xia, Q.; Yang, D.; Wang, Z.; Ren, Y.; Sun, B.; Feng, Q.; Qian, C. Multiphysical modeling for life analysis of lithium-ion battery pack in electric vehicles. *Renew. Sustain. Energy Rev.* **2020**, *131*, 109993. [[CrossRef](#)]
125. Rumpf, K.; Rheinfeld, A.; Schindler, M.; Keil, J.; Schua, T.; Jossen, A. Influence of Cell-to-Cell Variations on the Inhomogeneity of Lithium-Ion Battery Modules. *J. Electrochem. Soc.* **2018**, *165*, A2587–A2607. [[CrossRef](#)]
126. Yang, N.; Zhang, X.; Shang, B.; Li, G. Unbalanced discharging and aging due to temperature differences among the cells in a lithium-ion battery pack with parallel combination. *J. Power Sources* **2016**, *306*, 733–741. [[CrossRef](#)]
127. Mendoza, H.; Roberts, S.A.; Brunini, V.E.; Grillet, A.M. Mechanical and Electrochemical Response of a LiCoO₂ Cathode using Reconstructed Microstructures. *Electrochim. Acta* **2016**, *190*, 1–15. [[CrossRef](#)]
128. Lee, Y.K. Effect of transition metal ions on solid electrolyte interphase layer on the graphite electrode in lithium ion battery. *J. Power Sources* **2021**, *484*, 229270. [[CrossRef](#)]
129. Lee, Y.K.; Song, J.; Park, J. Multi-scale coupled mechanical-electrochemical modeling for study on stress generation and its impact on multi-layered electrodes in lithium-ion batteries. *Electrochim. Acta* **2021**, *389*, 138682. [[CrossRef](#)]

130. Krewer, U.; Röder, F.; Harinath, E.; Braatz, R.D.; Bedürftig, B.; Findeisen, R. Review—Dynamic Models of Li-Ion Batteries for Diagnosis and Operation: A Review and Perspective. *J. Electrochem. Soc.* **2018**, *165*, A3656–A3673. [[CrossRef](#)]
131. Rodríguez, A.; Plett, G.L.; Trimboli, M.S. Comparing four model-order reduction techniques, applied to lithium-ion battery-cell internal electrochemical transfer functions. *eTransportation* **2019**, *1*, 100009. [[CrossRef](#)]
132. Lyu, C.; Song, Y.; Zheng, J.; Luo, W.; Hinds, G.; Li, J.; Wang, L. In situ monitoring of lithium-ion battery degradation using an electrochemical model. *Appl. Energy* **2019**, *250*, 685–696. [[CrossRef](#)]
133. Wang, Y.; Li, J.; Zhang, J.; Pecht, M. Lithium-iron-phosphate battery electrochemical modelling under a wide range of ambient temperatures. *J. Electroanal. Chem.* **2021**, *882*, 115041. [[CrossRef](#)]
134. Li, X.; Huang, Z.; Tian, J.; Tian, Y. State-of-charge estimation tolerant of battery aging based on a physics-based model and an adaptive cubature Kalman filter. *Energy* **2021**, *220*, 119767. [[CrossRef](#)]
135. Ouyang, M.; Feng, X.; Han, X.; Lu, L.; Li, Z.; He, X. A dynamic capacity degradation model and its applications considering varying load for a large format Li-ion battery. *Appl. Energy* **2016**, *165*, 48–59. [[CrossRef](#)]
136. Smith, K.; Gasper, P.; Colclasure, A.M.; Shimonishi, Y.; Yoshida, S. Lithium-Ion Battery Life Model with Electrode Cracking and Early-Life Break-in Processes. *J. Electrochem. Soc.* **2021**, *168*, 100530. [[CrossRef](#)]
137. Zhang, X.; Chumakov, S.; Li, X.; Klinsmann, M.; Kim, S.U.; Linder, C.; Christensen, J. An Electro-chemo-thermo-mechanical Coupled Three-dimensional Computational Framework for Lithium-ion Batteries. *J. Electrochem. Soc.* **2020**, *167*, 160542. [[CrossRef](#)]
138. Qi, C.; Zhu, Y.; Gao, F.; Yang, K.; Jiao, Q. Mathematical model for thermal behavior of lithium ion battery pack under overcharge. *Int. J. Heat Mass Transf.* **2018**, *124*, 552–563. [[CrossRef](#)]
139. Chen, F.; Huang, R.; Wang, C.; Yu, X.; Liu, H.; Wu, Q.; Qian, K.; Bhagat, R. Air and PCM cooling for battery thermal management considering battery cycle life. *Appl. Therm. Eng.* **2020**, *173*, 115154. [[CrossRef](#)]
140. Yamanaka, T.; Takagishi, Y.; Yamaue, T. An Electrochemical-Thermal Model for Lithium-Ion Battery Packs during Driving of Battery Electric Vehicles. *J. Electrochem. Soc.* **2021**, *168*, 050545. [[CrossRef](#)]
141. Tran, N.T.; Farrell, T.; Vilathgamuwa, M.; Choi, S.S.; Li, Y. A Computationally Efficient Coupled Electrochemical-Thermal Model for Large Format Cylindrical Lithium Ion Batteries. *J. Electrochem. Soc.* **2019**, *166*, A3059–A3071. [[CrossRef](#)]
142. Song, W.; Chen, M.; Bai, F.; Lin, S.; Chen, Y.; Feng, Z. Non-uniform effect on the thermal/aging performance of Lithium-ion pouch battery. *Appl. Therm. Eng.* **2018**, *128*, 1165–1174. [[CrossRef](#)]
143. Liu, X.; Ai, W.; Naylor Marlow, M.; Patel, Y.; Wu, B. The effect of cell-to-cell variations and thermal gradients on the performance and degradation of lithium-ion battery packs. *Appl. Energy* **2019**, *248*, 489–499. [[CrossRef](#)]
144. Tian, Y.; Huang, Z.; Li, X.; Tian, J. Parallel-connected battery module modeling based on physical characteristics in multiple domains and heterogeneous characteristic analysis. *Energy* **2022**, *239*, 122181. [[CrossRef](#)]
145. Jia, Y.; Uddin, M.; Li, Y.; Xu, J. Thermal runaway propagation behavior within 18,650 lithium-ion battery packs: A modeling study. *J. Energy Storage* **2020**, *31*, 101668. [[CrossRef](#)]
146. Mevawalla, A.; Panchal, S.; Tran, M.K.; Fowler, M.; Fraser, R. One dimensional fast computational partial differential model for heat transfer in lithium-ion batteries. *J. Energy Storage* **2021**, *37*, 102471. [[CrossRef](#)]
147. Abada, S.; Petit, M.; Lecocq, A.; Marlair, G.; Sauvart-Moynot, V.; Huet, F. Combined experimental and modeling approaches of the thermal runaway of fresh and aged lithium-ion batteries. *J. Power Sources* **2018**, *399*, 264–273. [[CrossRef](#)]
148. Jia, Y.; Gao, X.; Mouillet, J.B.; Terrier, J.M.; Lombard, P.; Xu, J. Effective thermo-electro-mechanical modeling framework of lithium-ion batteries based on a representative volume element approach. *J. Energy Storage* **2021**, *33*, 102090. [[CrossRef](#)]
149. Hosseinzadeh, E.; Marco, J.; Jennings, P. Combined electrical and electrochemical-thermal model of parallel connected large format pouch cells. *J. Energy Storage* **2019**, *22*, 194–207. [[CrossRef](#)]
150. Chalise, D.; Shah, K.; Prasher, R.; Jain, A. Conjugate Heat Transfer Analysis of Thermal Management of a Li-Ion Battery Pack. *J. Electrochem. Energy Convers. Storage* **2018**, *15*, 1–8. [[CrossRef](#)]
151. Lamrani, B.; Lebrouhi, B.E.; Khattari, Y.; Kousksou, T. A simplified thermal model for a lithium-ion battery pack with phase change material thermal management system. *J. Energy Storage* **2021**, *44*, 103377. [[CrossRef](#)]
152. Kim, M.; Chun, H.; Kim, J.; Kim, K.; Yu, J.; Kim, T.; Han, S. Data-efficient parameter identification of electrochemical lithium-ion battery model using deep Bayesian harmony search. *Appl. Energy* **2019**, *254*, 113644. [[CrossRef](#)]
153. Li, Y.; Zhou, Z.; Wu, W.T. Three-dimensional thermal modeling of Li-ion battery cell and 50 V Li-ion battery pack cooled by mini-channel cold plate. *Appl. Therm. Eng.* **2019**, *147*, 829–840. [[CrossRef](#)]
154. Gottapu, M.; Goh, T.; Kaushik, A.; Adiga, S.P.; Bharathraj, S.; Patil, R.S.; Kim, D.; Ryu, Y. Fully coupled simplified electrochemical and thermal model for series-parallel configured battery pack. *J. Energy Storage* **2021**, *36*, 102424. [[CrossRef](#)]
155. Zheng, L.; Zhang, L.; Zhu, J.; Wang, G.; Jiang, J. Co-estimation of state-of-charge, capacity and resistance for lithium-ion batteries based on a high-fidelity electrochemical model. *Appl. Energy* **2016**, *180*, 424–434. [[CrossRef](#)]
156. Xia, Q.; Wang, Z.; Ren, Y.; Sun, B.; Yang, D.; Feng, Q. A reliability design method for a lithium-ion battery pack considering the thermal disequilibrium in electric vehicles. *J. Power Sources* **2018**, *386*, 10–20. [[CrossRef](#)]
157. Li, W.; Zhu, J.; Xia, Y.; Gorji, M.B.; Wierzbicki, T. Data-Driven Safety Envelope of Lithium-Ion Batteries for Electric Vehicles. *Joule* **2019**, *3*, 2703–2715. [[CrossRef](#)]
158. Zhang, X.; Li, P.; Huang, B.; Zhang, H. Numerical investigation on the thermal behavior of cylindrical lithium-ion batteries based on the electrochemical-thermal coupling model. *Int. J. Heat Mass Transf.* **2022**, *199*, 123449. [[CrossRef](#)]

159. Tu, H.; Moura, S.; Wang, Y.; Fang, H. Integrating physics-based modeling with machine learning for lithium-ion batteries. *Appl. Energy* **2023**, *329*, 120289. [[CrossRef](#)]
160. Appiah, W.A.; Busk, J.; Vegge, T.; Bhowmik, A. Sensitivity analysis methodology for battery degradation models. *Electrochim. Acta* **2023**, *439*, 141430. [[CrossRef](#)]
161. Dubarry, M.; Baure, G. Perspective on Commercial Li-ion Battery Testing, Best Practices for Simple and Effective Protocols. *Electronics* **2020**, *9*, 152. [[CrossRef](#)]
162. Baure, G.; Dubarry, M. Synthetic vs. Real driving cycles: A comparison of electric vehicle battery degradation. *Batteries* **2019**, *5*. [[CrossRef](#)]
163. Pfriem, M.; Gauterin, F. Development of real-world driving cycles for battery electric vehicles. *World Electr. Veh. J.* **2016**, *8*, 14–24. [[CrossRef](#)]
164. Wang, D.; Coignard, J.; Zeng, T.; Zhang, C.; Saxena, S. Quantifying electric vehicle battery degradation from driving vs. vehicle-to-grid services. *J. Power Sources* **2016**, *332*, 193–203. [[CrossRef](#)]
165. Diao, W.; Saxena, S.; Pecht, M. Accelerated cycle life testing and capacity degradation modeling of LiCoO₂-graphite cells. *J. Power Sources* **2019**, *435*, 226830. [[CrossRef](#)]
166. Pastor-Fernández, C.; Uddin, K.; Chouchelamane, G.H.; Widanage, W.D.; Marco, J. A Comparison between Electrochemical Impedance Spectroscopy and Incremental Capacity-Differential Voltage as Li-ion Diagnostic Techniques to Identify and Quantify the Effects of Degradation Modes within Battery Management Systems. *J. Power Sources* **2017**, *360*, 301–318. [[CrossRef](#)]
167. Al-Zubaidi R-Smith, N.; Leitner, M.; Alic, I.; Toth, D.; Kasper, M.; Romio, M.; Surace, Y.; Jahn, M.; Kienberger, F.; Ebner, A.; et al. Assessment of lithium ion battery ageing by combined impedance spectroscopy, functional microscopy and finite element modelling. *J. Power Sources* **2021**, *512*, 230459. [[CrossRef](#)]
168. Raj, T.; Wang, A.A.; Monroe, C.W.; Howey, D.A. Investigation of Path-Dependent Degradation in Lithium-Ion Batteries**. *Batter. Supercaps* **2020**, *3*, 1377–1385. [[CrossRef](#)]

Disclaimer/Publisher's Note: The statements, opinions and data contained in all publications are solely those of the individual author(s) and contributor(s) and not of MDPI and/or the editor(s). MDPI and/or the editor(s) disclaim responsibility for any injury to people or property resulting from any ideas, methods, instructions or products referred to in the content.